

# VT-Aircraft: Simulation of Aircraft Motion During Vortex Tube Encounters

Technical Documentation and Code Description

Nils T. Basse\*

Python implementation with AI assistance (Claude, Anthropic)

21st of March 2026

## Abstract

This document provides a complete technical description of the VT-Aircraft Python package, which simulates the three-dimensional motion of an aircraft (or drone) encountering one or more atmospheric vortex tubes (VTs). The code extends the MATLAB implementation described in Basse (2020, *Meteorol. Atmos. Phys.*, 132:401–411) and the associated draft manuscript (2019). Key improvements include: (i) 4th-order Runge–Kutta (RK4) time integration replacing forward Euler; (ii) a single-phase design with analytical trim replacing the two-phase stabilisation approach; (iii) derivation of the Brunt–Väisälä (B-V) calibration constants as  $\sqrt{\gamma/(\gamma - n)}$  from the polytropic index and ratio of specific heats; (iv) a thrust-specific fuel consumption (TSFC) model; (v) multiple vortex tube support; (vi) 28 diagnostic plots including turbulence severity metrics and aeroacoustic sound pressure level (SPL) spectrograms. All damping, fuel consumption, and atmospheric model parameters are derived from fundamental quantities without free fitting constants. A structural analogy between VT encounters and edge-localised modes (ELMs) in fusion plasmas is identified, with a mathematical correspondence between the vortex acceleration  $\frac{1}{2}\boldsymbol{\omega} \times \mathbf{v}$  and the magnetohydrodynamic (MHD) Lorentz acceleration  $\mathbf{j} \times \mathbf{B}/\rho$ .

## Contents

<b>1</b>	<b>Introduction</b>	<b>3</b>
<b>2</b>	<b>Physical Model</b>	<b>3</b>
2.1	Polytropic Atmosphere . . . . .	3
2.1.1	Derivation of the Polytropic Index . . . . .	4
2.1.2	State Variables . . . . .	4
2.1.3	Atmospheric Stability . . . . .	4
2.2	Vortex Tube Geometry . . . . .	5
2.2.1	Inside/Outside Test . . . . .	5
2.3	Aircraft Configuration . . . . .	5
2.3.1	Trim State . . . . .	6
2.3.2	Fuel Consumption . . . . .	6
2.4	Equations of Motion . . . . .	6
2.4.1	Damping Model . . . . .	7
2.4.2	Drag Polar (Optional) . . . . .	7
2.4.3	Time Integration . . . . .	7
2.4.4	Point vs. Area Model . . . . .	7

---

\*RISE Research Institutes of Sweden, Brinellgatan 4, 504 62 Borås, Sweden. E-mail: nils.basse@ri.se

2.5	Aircraft Oscillation Frequency . . . . .	8
2.6	Aeroacoustic Model . . . . .	9
<b>3</b>	<b>Results</b>	<b>9</b>
3.1	Summary of Results . . . . .	9
3.2	Diagnostic Plots . . . . .	10
3.2.1	Trajectory and Kinematics . . . . .	10
3.2.2	Turbulence Loads and Passenger Comfort . . . . .	10
3.2.3	Oscillation Physics . . . . .	11
3.2.4	Energy Budget . . . . .	13
3.2.5	Spectral Analysis and Aeroacoustics . . . . .	13
3.2.6	Flight Dynamics and Fuel . . . . .	14
3.2.7	Sound Generation . . . . .	15
3.2.8	Area Fractions (Area Model Only) . . . . .	15
<b>4</b>	<b>Discussion</b>	<b>16</b>
4.1	Comparison with Previous Work . . . . .	16
4.2	Analogy with Edge-Localised Modes in Fusion Plasmas . . . . .	17
4.2.1	Mathematical Structure: Vortex Force Analogy . . . . .	17
4.2.2	ELM Types and VT Encounter Patterns . . . . .	19
4.2.3	Key Differences . . . . .	20
4.3	Model Limitations . . . . .	20
4.4	Future Research Directions . . . . .	21
<b>5</b>	<b>Conclusions</b>	<b>22</b>
<b>A</b>	<b>Code Structure</b>	<b>22</b>
A.1	Algorithm and Dataflow . . . . .	23
A.1.1	Algorithmic Description . . . . .	23
A.2	Key Classes . . . . .	25
<b>B</b>	<b>Dependencies and Installation</b>	<b>25</b>
<b>C</b>	<b>Configuration Reference</b>	<b>26</b>
<b>D</b>	<b>Predefined Cases</b>	<b>26</b>
<b>E</b>	<b>Postprocessing Quantities</b>	<b>27</b>
<b>F</b>	<b>Diagnostic Plots</b>	<b>28</b>
<b>G</b>	<b>Physics-Derived vs. Configured Parameters</b>	<b>30</b>
<b>H</b>	<b>Validation</b>	<b>30</b>
<b>I</b>	<b>Errata for Basse (2020)</b>	<b>30</b>
I.1	Typographical Error in Equation (4) . . . . .	31
I.2	Out-of-Plane Axis Symbol in Figure 3 (Wing Panel) . . . . .	31
I.3	Viewing Convention in Figure 2 . . . . .	31
I.4	Summary . . . . .	31

## 1 Introduction

Aviation turbulence has significant impacts on flight comfort, safety, and operating costs [1]. While turbulence arises from many sources (convection, mountain waves, jet streams), a subset of events—particularly clear-air turbulence (CAT)—can be described as interactions between an aircraft and coherent atmospheric vortex tubes (VTs). Horizontal vortex tubes have been identified during CAT events [2], with physical formation mechanisms described by Roach [3] and Kaplan et al. [4]. The theoretical framework for vortex tube dynamics follows from classical hydrodynamics [5, 6].

The modelling approach taken here follows the framework established in Basse [7], where the aircraft acceleration due to a VT is derived from the hydrodynamic impulse [8]:

$$\mathbf{a}_{\text{AC}} = \frac{1}{2}\boldsymbol{\omega} \times \mathbf{v}_{\text{AC}}, \quad (1)$$

where  $\boldsymbol{\omega}$  is the vorticity of the vortex tube and  $\mathbf{v}_{\text{AC}}$  is the aircraft (AC) velocity. This expression models the VT as a region of solid-body rotation that imparts an impulsive acceleration to the aircraft as it transits through.

The original MATLAB code (`rev1_aircraft_eq_of_motion.m`,  $\sim 1700$  lines) [9] used forward Euler time integration and a two-phase approach: a long stabilisation phase to damp out transients from imperfect initial conditions, followed by the actual VT encounter. The present Python implementation replaces this with:

- Classical 4th-order Runge–Kutta (RK4) integration for improved accuracy.
- A single-phase design with analytically computed trim state using exact drag and lift coefficients ( $C_d$ ,  $C_l$ ) at initialisation ( $t = 0$ ), eliminating the need for artificial stabilisation.
- Physics-derived expressions for all calibration constants, damping coefficients, and fuel consumption parameters.
- Support for multiple co- or counter-rotating vortex tubes.
- Both point and finite-area aircraft models.
- Comprehensive postprocessing producing 28 diagnostic plots.

The code is structured as a modular Python package (11 files,  $\sim 2800$  lines) [10] that runs in any Python 3.8+ environment, with particular support for Anaconda/Spyder through the `run_spyder.py` script.

The remainder of this document is organised as follows. Section 2 describes the physical model: atmosphere, vortex tube geometry, aircraft configuration, equations of motion (EOM), the aircraft oscillation frequency, and the aeroacoustic model. Section 3 provides representative results comparing the point and finite-area aircraft models, including diagnostic plots and spectrogram analysis. Section 4 discusses the analogy with ELMs in fusion plasmas, model limitations, and future research directions. Section 5 summarises the conclusions. The appendices provide: code structure and algorithmic description (Appendix A), dependencies and installation (Appendix B), configuration reference (Appendix C), predefined cases (Appendix D), postprocessing quantities (Appendix E), diagnostic plot catalogue (Appendix F), physics-derived vs. configured parameters (Appendix G), validation (Appendix H), and errata for the 2020 paper (Appendix I).

## 2 Physical Model

### 2.1 Polytropic Atmosphere

The atmosphere is modelled as a polytropic gas with altitude-dependent gravity:

$$g(z) = \frac{G m_{\text{Earth}}}{(r_{\text{Earth}} + z)^2}, \quad (2)$$

where  $G = 6.67384 \times 10^{-11} \text{ m}^3/(\text{kg}\cdot\text{s}^2)$ ,  $m_{\text{Earth}} = 5.9722 \times 10^{24} \text{ kg}$ , and  $r_{\text{Earth}} = 6.371 \times 10^6 \text{ m}$ .

### 2.1.1 Derivation of the Polytrropic Index

A key improvement over the original code is that the polytrropic index  $n$  is *derived* from the International Standard Atmosphere (ISA) tropospheric lapse rate  $\Lambda = -6.5$  K/km [11], rather than being independently specified from Nakayama [12]. For a polytrropic atmosphere, the temperature gradient is:

$$\frac{dT}{dz} = -T_0 \frac{n-1}{n} \frac{\rho_0 g}{p_0} = \Lambda. \quad (3)$$

Solving for  $n$ :

$$n = \frac{1}{1 + \Lambda p_0 / (T_0 \rho_0 g_{\text{SL}})} = 1.2346, \quad (4)$$

which matches Nakayama's value of 1.235 to 0.03%. This ensures thermodynamic self-consistency:  $n$ ,  $\gamma$ , and the lapse rate are not independent parameters—specifying any two determines the third.

### 2.1.2 State Variables

The density, temperature, and pressure at altitude  $z$  are:

$$\rho(z) = \rho_0 f^{1/(n-1)}, \quad (5)$$

$$T(z) = T_0 f, \quad (6)$$

$$p(z) = R_{\text{air}} \rho(z) T(z), \quad (7)$$

where  $f \equiv 1 - \alpha(z) z$  and  $\alpha(z) = \frac{n-1}{n} \frac{\rho_0 g(z)}{p_0}$ . Note that the code uses the altitude-dependent gravity  $g(z)$  in  $\alpha$  for improved accuracy over the standard constant- $g$  polytrropic model; the effect is small ( $g$  varies by 0.3% at 10 km). Sea-level (SL) reference values are  $\rho_0 = 1.225$  kg/m<sup>3</sup>,  $p_0 = 101\,325$  Pa,  $T_0 = 288.15$  K, and  $R_{\text{air}} = 287.058$  J/(kg·K). Additional derived properties:

$$R/c_p = (\gamma - 1)/\gamma = 2/7 \approx 0.2857, \quad c_p = R_{\text{air}}/(R/c_p) = 1004.7 \text{ J}/(\text{kg}\cdot\text{K}). \quad (8)$$

The speed of sound, potential temperature, and dynamic viscosity are:

$$c = \sqrt{\gamma p/\rho}, \quad (9)$$

$$\theta = T (p_0/p)^{R/c_p}, \quad (10)$$

$$\mu = \frac{1.458 \times 10^{-6} T^{3/2}}{110.4 + T} + E_0 + E_1 \rho + E_2 \rho^2, \quad (11)$$

where  $E_0 = -5.516 \times 10^{-8}$ ,  $E_1 = 1.1 \times 10^{-8}$ ,  $E_2 = 5.565 \times 10^{-11}$  (SI units) are Zagarola's residual density corrections to Sutherland's formula [13].

### 2.1.3 Atmospheric Stability

The Brunt-Väisälä (B-V) frequency for a fluid parcel is [14]:

$$N^2 = \frac{g}{\theta} \frac{d\theta}{dz}. \quad (12)$$

For the polytrropic model,  $d\theta/dz$  is computed analytically from the known profiles of  $T(z)$  and  $p(z)$ .

The lapse rates are:

$$\Gamma_{\text{model}} = \frac{dT}{dz} = -\frac{n-1}{n} \frac{\rho_0 g T_0}{p_0} \approx -6.5 \text{ K/km}, \quad (13)$$

$$\Gamma_{\text{dry}} = -g/c_p \approx -9.75 \text{ K/km}. \quad (14)$$

Since  $|\Gamma_{\text{model}}| < |\Gamma_{\text{dry}}|$ , the atmosphere is statically stable.

## 2.2 Vortex Tube Geometry

The vortex tube is a finite cylinder of radius  $R$  and width  $W$  (axial extent), rotating as a solid body with angular velocity  $\Omega$ . The VT dimensions are determined from the vortex/aircraft area ratio  $r_A$  [7]:

$$R = \sqrt{r_A L H / \pi}, \quad W = \frac{SC}{2} \sqrt{r_A \pi / (LH)}, \quad (15)$$

where  $L$ ,  $H$  are fuselage length and height, and  $S$ ,  $C$  are wing span and chord. For the default A330-200 parameters and  $r_A = 10$ :  $R = 33.9$  m,  $W = 53.2$  m.

The angular velocity is set by the desired peak acceleration:

$$\Omega = \frac{a_g g_{\text{init}}}{v_{\text{init}}}, \quad (16)$$

where the acceleration fraction  $a_g = 0.5$  represents a significant turbulence event [15].

For a general vortex orientation defined by azimuthal angle  $\phi$  and polar angle  $\theta$ , the vorticity components are [7]:

$$\omega_x = -2\Omega \sin \theta \cos \phi, \quad \omega_y = -2\Omega \sin \theta \sin \phi, \quad \omega_z = -2\Omega \cos \theta. \quad (17)$$

The baseline orientation  $\phi = \theta = \pi/2$  gives a transverse horizontal VT with  $\omega_y = -2\Omega$  and  $\omega_x = \omega_z = 0$ .

### 2.2.1 Inside/Outside Test

The original MATLAB code used a Delaunay convex hull triangulation to determine whether a point is inside the VT. This introduced  $\sim 0.7\%$  volume error. The Python code replaces this with an exact analytical cylinder test: a point  $\mathbf{p}$  is inside the VT if and only if:

$$|\text{proj}_{\hat{\mathbf{a}}}(\mathbf{p} - \mathbf{c})| \leq W/2 \quad \text{and} \quad |\mathbf{p} - \mathbf{c} - \text{proj}_{\hat{\mathbf{a}}}(\mathbf{p} - \mathbf{c})|^2 \leq R^2, \quad (18)$$

where  $\mathbf{c}$  is the cylinder centre and  $\hat{\mathbf{a}}$  is its axis direction. This test is vectorised for the area model and preceded by a bounding-box pre-check that provides a  $2.7\times$  speedup.

## 2.3 Aircraft Configuration

Default parameters approximate an Airbus A330-200 [16]:

Parameter	Symbol	Value	Unit
Wing span	$S$	60	m
Wing chord	$C$	6	m
Wing area	$A_{\text{wing}}$	360	m <sup>2</sup>
Fuselage length	$L$	60	m
Fuselage height	$H$	6	m
Aspect ratio	AR (aspect ratio) = $S/C$	10	—
Initial mass	$m_{\text{init}}$	230 000	kg
Initial speed	$v_{\text{init}}$	222.2	m/s (800 km/h)
Initial altitude	$z_{\text{init}}$	10 000	m
Sea-level max thrust	$\mathcal{T}_{\text{SL}}$	600 000	N
Thrust factor	$\mathcal{T}_f$	0.5	—

A small electric drone preset (`small_drone()`) is also provided for unmanned aircraft system (UAS) studies.

### 2.3.1 Trim State

At the initial conditions, the drag and lift coefficients are determined by force balance (thrust = drag, lift = weight):

$$C_d = \frac{2 \mathcal{T}_{\text{init}}}{\rho_{\text{init}} v_{\text{init}}^2 A_{\text{wing}}}, \quad C_l = \frac{2 m_{\text{init}} g_{\text{init}}}{\rho_{\text{init}} v_{\text{init}}^2 A_{\text{wing}}}, \quad (19)$$

where  $\mathcal{T}_{\text{init}} = \mathcal{T}_f \mathcal{T}_{\text{SL}} \rho_{\text{init}} / \rho_0$  is the thrust at cruise altitude. This gives  $C_d = 0.02755$  and  $C_l = 0.6124$  for the A330 defaults. The aircraft starts exactly in equilibrium, eliminating the need for a stabilisation phase.

### 2.3.2 Fuel Consumption

Fuel consumption uses a thrust-specific fuel consumption (TSFC) model:

$$\frac{dm}{dt} = -\text{TSFC} \times \mathcal{T}(t), \quad (20)$$

where  $\text{TSFC} = 15 \times 10^{-6} \text{ kg}/(\text{N}\cdot\text{s}) = 15 \text{ mg}/(\text{N}\cdot\text{s})$  is a characteristic property of modern high-bypass turbofan engines. This replaces the original constant-per-distance model ( $F = 6 \text{ g}/\text{m}$ ). At 10 km cruise, the TSFC model gives  $\sim 5500 \text{ kg}/\text{hr}$  fuel burn, consistent with published A330 data. The original  $F = 6 \text{ g}/\text{m}$  implied  $\text{TSFC} = 13.2 \text{ mg}/(\text{N}\cdot\text{s})$ , which is on the low side of the published range (15–17  $\text{mg}/(\text{N}\cdot\text{s})$ ).

A key advantage of the TSFC model is that fuel burn rate varies correctly with altitude (lower density  $\rightarrow$  less thrust required  $\rightarrow$  less fuel consumed) and with mass (lighter aircraft  $\rightarrow$  less lift needed  $\rightarrow$  less thrust  $\rightarrow$  less fuel). Set  $\text{TSFC} = 0$  for electric drones or no-fuel-burn cases.

## 2.4 Equations of Motion

The state vector is  $\mathbf{s} = [x, y, z, v_x, v_y, v_z]$ . Outside the VT, the EOM are:

$$a_x = \mathcal{T}/m - A_d v_x^2, \quad (21)$$

$$a_y = -c_{1,y} v_y/m, \quad (22)$$

$$a_z = A_l v_x^2 - g - c_{1,z} v_z/m, \quad (23)$$

where:

$$A_d = \frac{C_d \rho A_{\text{wing}}}{2m}, \quad A_l = \frac{C_l \rho A_{\text{wing}}}{2m}. \quad (24)$$

The drag term uses  $v_x^2$  rather than  $|\mathbf{v}|^2$ . This is a standard small-perturbation approximation, valid when  $v_y, v_z \ll v_x$  (typically 1.5 m/s vs. 222 m/s).

The thrust includes a mass-correction factor modelling autopilot throttle reduction as fuel burns:

$$\mathcal{T} = \frac{m}{m_{\text{init}}} \mathcal{T}_f \mathcal{T}_{\text{SL}} \frac{\rho}{\rho_0}. \quad (25)$$

This is a *control model* (the autopilot reduces throttle to prevent acceleration as the aircraft becomes lighter), not an engine physics model.

Inside the VT, the vortex-induced acceleration from Eq. (1) is added:

$$a_x += \frac{1}{2}(\omega_y v_z - \omega_z v_y), \quad (26)$$

$$a_y += \frac{1}{2}(\omega_z v_x - \omega_x v_z), \quad (27)$$

$$a_z += \frac{1}{2}(\omega_x v_y - \omega_y v_x). \quad (28)$$

For multiple VTs, the contributions from each are summed.

### 2.4.1 Damping Model

Three named damping modes are provided:

Mode	CLI flag	Formula	$c_1$ (A330)	Half-life $t_{1/2}$
<b>aero</b> (default)	-damping <b>aero</b>	$c_1 = \rho v C_d A_{\text{wing}}$	912 kg/s	175 s
<b>strong</b>	-damping <b>strong</b>	$c_1 = m a_{\text{VT}}/v$	5066 kg/s	31 s
<b>none</b>	-damping <b>none</b>	$c_1 = 0$	0	$\infty$

The phugoid period and damping ratio [17]:

$$T_{\text{ph}} = \sqrt{2} \pi v/g, \quad \zeta = C_d/(\sqrt{2} C_l). \quad (29)$$

### 2.4.2 Drag Polar (Optional)

An optional drag polar couples  $C_d$  to  $C_l$  through the wing geometry:

$$C_d = C_{d,0} + \frac{C_l^2}{\pi \text{AR} e}, \quad (30)$$

where  $e \approx 0.8$  is the Oswald span efficiency factor. When enabled (`USE_DRAG_POLAR = True`), this implements a variable angle of attack (AoA) autopilot that adjusts  $C_l$  to maintain level flight. This is a fundamentally different physical model: the autopilot suppresses the oscillation and produces a permanent altitude shift instead. With fixed angle of attack (the default),  $C_l$  and  $C_d$  are constants.

### 2.4.3 Time Integration

The equations are integrated using the classical 4th-order Runge–Kutta method:

$$\mathbf{k}_1 = \mathbf{F}(\mathbf{s}_k), \quad \mathbf{k}_2 = \mathbf{F}(\mathbf{s}_k + \frac{1}{2} \Delta t \mathbf{k}_1), \quad (31)$$

$$\mathbf{k}_3 = \mathbf{F}(\mathbf{s}_k + \frac{1}{2} \Delta t \mathbf{k}_2), \quad \mathbf{k}_4 = \mathbf{F}(\mathbf{s}_k + \Delta t \mathbf{k}_3), \quad (32)$$

$$\mathbf{s}_{k+1} = \mathbf{s}_k + \frac{\Delta t}{6} (\mathbf{k}_1 + 2\mathbf{k}_2 + 2\mathbf{k}_3 + \mathbf{k}_4). \quad (33)$$

Atmospheric quantities ( $g$ ,  $\rho$ ,  $T$ ) are evaluated at the start of each step and held constant across the four sub-evaluations (operator splitting). This is justified because the altitude change within one step ( $\Delta z \sim v_z \Delta t \sim 0.15$  m for  $\Delta t = 0.1$  s) causes negligible atmospheric variation ( $\Delta\rho/\rho \sim 10^{-6}$ ).

### 2.4.4 Point vs. Area Model

In the **point model**, the VT inside/outside test is applied at the aircraft centre of mass (CoM). In the **area model**, the wing (in the  $xy$ -plane) and fuselage (in the  $xz$ -plane) are discretised on grids with spacing  $\Delta y = \Delta z = 0.5$  m. The area fractions inside the VT are computed for each surface, and the vortex acceleration is scaled accordingly [7]:

- $a_z$  (vertical) is scaled by the wing fraction (reflecting lift perturbation),
- $a_y$  (lateral) is scaled by the fuselage fraction (reflecting side force),
- $a_x$  (longitudinal) is scaled by the average of wing and fuselage fractions.

## 2.5 Aircraft Oscillation Frequency

A key finding of this work is that the observed post-VT oscillation is not the Brunt–Väisälä (B-V) frequency of a fluid parcel but a distinct *aircraft oscillation* arising from lift-density coupling. When an aircraft is displaced vertically by  $\delta z$ , the change in air density alters the aerodynamic lift. From the lift equation  $L = \frac{1}{2}\rho v^2 C_L A$  and the trim condition  $\frac{1}{2}\rho v^2 C_L A = mg$ :

$$\frac{\partial L}{\partial z} = \frac{1}{2}v^2 C_L A \frac{d\rho}{dz} = \frac{mg}{\rho} \frac{d\rho}{dz}. \quad (34)$$

Since  $d\rho/dz < 0$ , lift decreases with altitude—this is the restoring mechanism. The restoring acceleration per unit displacement is  $(1/m)(\partial L/\partial z)$ , giving an oscillation frequency:

$$\omega_{\text{aircraft}}^2 = -\frac{g}{\rho} \frac{d\rho}{dz}. \quad (35)$$

For the polytropic atmosphere, the density gradient is:

$$\frac{d\rho}{dz} = -\frac{\rho_0 \alpha}{(n-1)} f^{(2-n)/(n-1)}, \quad (36)$$

so:

$$\omega_{\text{aircraft}}^2 = \frac{g\alpha}{(n-1)f}. \quad (37)$$

The ratio of this frequency to the atmospheric B-V frequency is:

$$\frac{\omega_{\text{aircraft}}}{N_{\text{BV}}} = \sqrt{\frac{\gamma}{\gamma-n}} = \sqrt{\frac{1.4}{1.4-1.2346}} \approx 2.909. \quad (38)$$

This ratio is **altitude-independent**—it depends only on  $\gamma$  and  $n$ , which are properties of the gas and the atmosphere, not the flight altitude.

This analytical result replaces the empirical calibration constants from the draft paper [18]: the fitted divisor 2.893 and the reference potential temperature  $\theta_0 = 39.15$  K. The small differences (0.7% and 1.4%) are attributable to forward Euler integration noise in the original MATLAB calibration. We can verify:

$$\theta_0 = \frac{\gamma-n}{\gamma} \theta(z) = \frac{1.4-1.2346}{1.4} \times 327.6 \text{ K} = 38.7 \text{ K}, \quad (39)$$

matching the fitted value of 39.15 K to 1.4%.

**Physical interpretation:** An aircraft is not a buoyant fluid parcel. Its restoring mechanism comes from the *density dependence of aerodynamic lift*, which acts more strongly than buoyancy because the polytropic lapse rate ( $-6.5$  K/km) is less steep than the dry adiabatic lapse rate ( $-g/c_p = -9.75$  K/km). The atmosphere is stable but “less stable” for buoyancy than for lift-density coupling, so the aircraft oscillates faster.

Table 1: Characteristic oscillation periods at 10 km altitude.

Period	Value [s]	Mechanism	Source
B-V (fluid parcel)	526	Buoyancy restoring force	Eq. (12)
Aircraft oscillation	181	Lift-density coupling	Eq. (35), this work
Phugoid (Lanchester)	101	Speed-altitude exchange	Eq. (29)
Observed (FFT)	~179	Simulation output	RK4 result

## 2.6 Aeroacoustic Model

The acoustic radiation from an aircraft experiencing unsteady loading is modelled using the aeroacoustic dipole formula [19]. An aircraft is a compact body (size  $\ll$  acoustic wavelength) experiencing an unsteady force  $\mathbf{F}(t) = m \mathbf{a}(t)$ , where  $\mathbf{a}$  is the total acceleration. The far-field acoustic pressure at distance  $r$  is:

$$p'(r, t) = \frac{1}{4\pi c r} \frac{d|\mathbf{F}|}{dt} = \frac{m}{4\pi c r} \left| \frac{d\mathbf{a}}{dt} \right|. \quad (40)$$

The sound pressure level (SPL) is then:

$$\text{SPL} = 20 \log_{10} \left( \frac{|p'|}{p_{\text{ref}}} \right), \quad p_{\text{ref}} = 20 \mu\text{Pa}. \quad (41)$$

The time-frequency structure of the acoustic radiation is visualised using short-time Fourier transform (STFT) spectrograms of the signed acoustic pressure  $p'(t)$ , computed with Hanning-windowed segments. The power spectral density (PSD) is expressed in dB re  $(20 \mu\text{Pa})^2/\text{Hz}$ .

The compact-source assumption is well satisfied: at the oscillation frequency ( $f \sim 0.006$  Hz), the acoustic wavelength is  $\lambda = c/f \sim 50$  km, far exceeding the VT diameter ( $\sim 68$  m) or aircraft size ( $\sim 60$  m). Even at the VT encounter frequency ( $\sim 3$  Hz),  $\lambda \sim 100$  m.

## 3 Results

This section presents results for Case 1 (large transverse horizontal VT,  $r_A = 10$ ,  $\phi = \theta = \pi/2$ ), comparing the point model (left panels) and finite-area model (right panels) for an A330-200 aircraft with TSFC-based fuel consumption and aerodynamic damping. Unless otherwise noted, all figures show this side-by-side comparison with  $t_{\text{before}} = 500$  s and  $t_{\text{after}} = 2000$  s.

### 3.1 Summary of Results

Table 2 summarises the key quantitative differences between the two aircraft models.

Table 2: Comparison of point and area model results for Case 1.

Quantity	Point	Area	Change
VT transit duration [s]	0.20	0.50	+150%
Peak $v_z$ [m/s]	$\pm 1.5$	$\pm 1.0$	-33%
Peak $\Delta n$ [g]	0.50	0.44	-12%
Turbulence severity	Moderate	Moderate	—
Dose of discomfort (DoD) [m/s]	18.5	13.6	-26%
Oscillation period (FFT) [s]	179	179	identical
Damping e-folding time [s]	252	252	identical
Peak SPL at 100 m [dB]	$\sim 120$	$\sim 117$	-3 dB
Fuel consumed (2500 s) [kg]	3761	3761	identical
Final altitude shift [m]	+13.6	+13.6	identical

The area model reduces the peak loads by 12–33% because the VT does not envelop the entire aircraft simultaneously: the wing leading edge enters the VT before the centre of mass, and the trailing edge exits after it. This spreads the impulse over a longer time interval (0.50 s vs. 0.20 s), reducing the peak acceleration but preserving the total impulse. The post-VT oscillation period and damping are identical in both models, confirming that these are determined by the atmospheric density gradient and aerodynamic drag—not by the encounter geometry.

## 3.2 Diagnostic Plots

The simulation produces 28 diagnostic plots (see Appendix F). The following figures present the key results. Each figure shows the point model (left) and area model (right) for direct comparison.

### 3.2.1 Trajectory and Kinematics

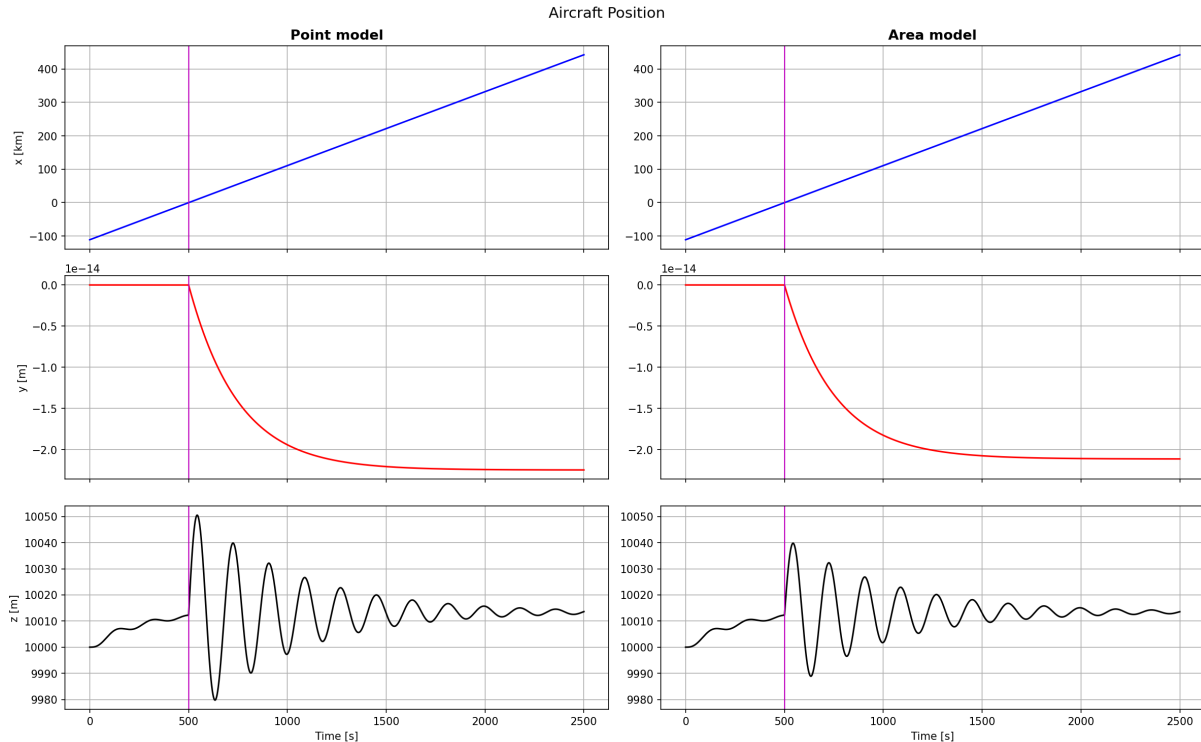


Figure 1: Aircraft position components  $x(t)$ ,  $y(t)$ ,  $z(t)$ : point model (left) vs. area model (right). Both models show identical forward progress and zero lateral drift ( $y \sim 10^{-14}$  m for Case 1). The  $z$ -component shows a damped oscillation with the same period ( $\sim 181$  s) in both models, but the area model has a smaller initial amplitude due to the reduced peak acceleration.

Figure 1 shows the three position components. The forward position  $x(t)$  increases linearly at  $\sim 222$  m/s with a slight deceleration from fuel-burn-induced drag changes. The lateral position  $y(t)$  remains at machine zero, confirming that Case 1 ( $\phi = \theta = \pi/2$ ) produces no spurious lateral motion. The vertical position  $z(t)$  shows the characteristic damped oscillation after the VT encounter at  $t \approx 500$  s.

Figure 2 is the single best summary plot. The damped oscillation in  $z(t)$  and  $v_z(t)$  is clearly visible in both models. The oscillation period is identical ( $\sim 181$  s), confirming that it is determined by the atmospheric lift-density coupling (Eq. 35), not the encounter geometry. The 33% reduction in peak  $v_z$  for the area model is the most prominent difference: the gradual immersion of the wing into the VT smooths the impulse.

Figure 3 shows the VT intersection status with a zoomed inset around the encounter. The longer transit time of the area model (0.50 s vs. 0.20 s) is clearly visible and explains the reduced peak loads: the same total momentum transfer is distributed over  $2.5\times$  the duration.

### 3.2.2 Turbulence Loads and Passenger Comfort

Figure 4 presents the turbulence severity metrics. Both models produce Moderate turbulence according to the International Civil Aviation Organization (ICAO)/Sharman classification [15] ( $\Delta n < 0.5$  g). The DoD [20] in the area model is 26% lower (13.6 m/s vs. 18.5 m/s), reflecting

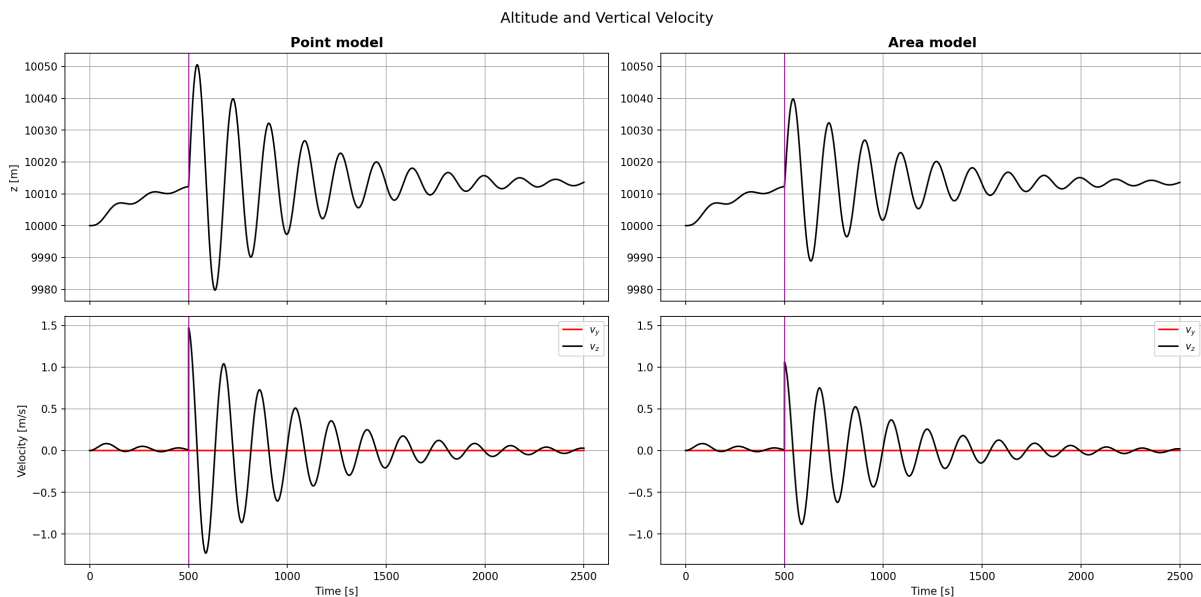


Figure 2: Altitude and vertical velocity: point model (left) vs. area model (right). The point model reaches  $\pm 1.5$  m/s peak vertical velocity; the area model reaches  $\pm 1.0$  m/s. Both oscillate at  $\sim 181$  s and damp with the same e-folding time (252 s). The altitude settles  $\sim 13.6$  m above the initial value due to fuel burn reducing mass.

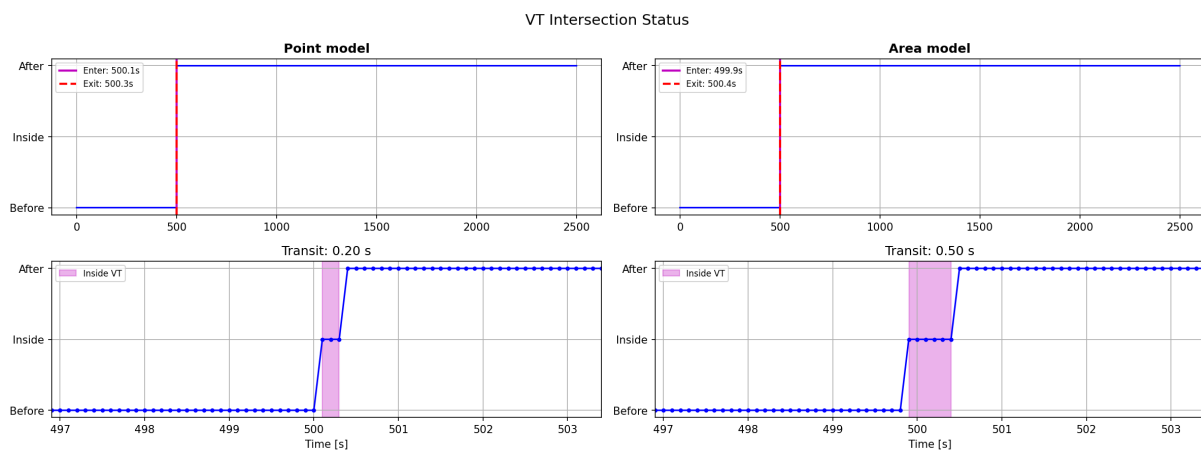


Figure 3: VT intersection status: point model (left) vs. area model (right). The top panels show the full timeline; the bottom panels zoom to the encounter. The point model transit lasts 0.20 s; the area model transit lasts 0.50 s because the wing span ( $S = 60$  m) exceeds the VT width ( $W = 53.2$  m), so parts of the aircraft enter the VT before the centre of mass and exit after it.

the integrated effect of the reduced oscillation amplitude over the full post-encounter period. The longitudinal ( $n_x$ ) and transverse ( $n_y$ ) load factors are three orders of magnitude smaller than  $\Delta n$ , confirming that the VT encounter is essentially a vertical perturbation for Case 1.

### 3.2.3 Oscillation Physics

Figure 5 compares the three characteristic periods. The observed fast Fourier transform (FFT) period ( $\sim 179$  s) closely matches the analytical aircraft oscillation period (181 s) in both models, confirming that the aircraft model (point vs. area) affects only the *amplitude*, not the *frequency*, of the post-VT oscillation.

Figure 6 confirms that the atmospheric properties (potential temperature, lapse rate, static

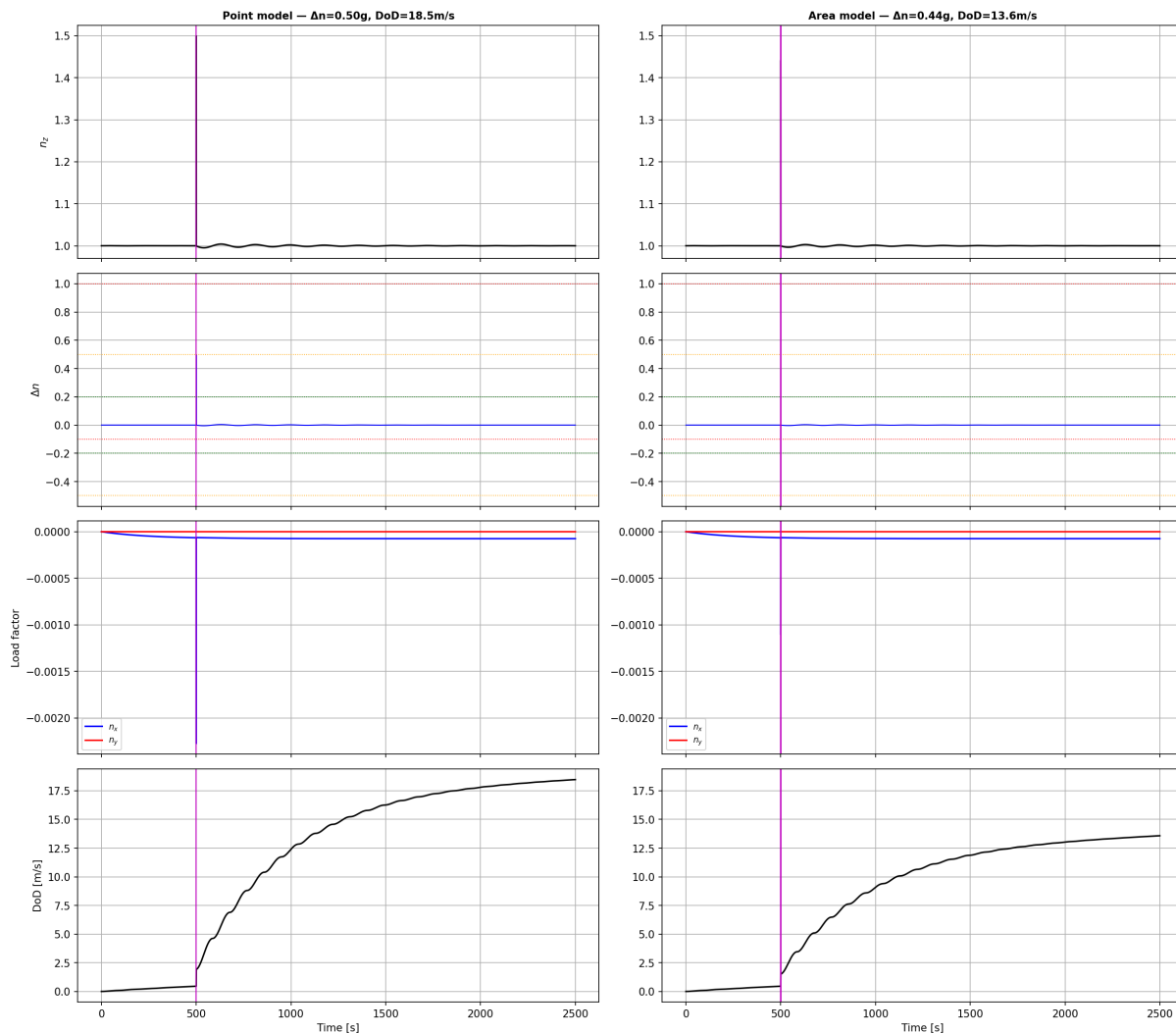


Figure 4: Turbulence g-loads: point model (left,  $\Delta n = 0.50$  g, DoD = 18.5 m/s) vs. area model (right,  $\Delta n = 0.44$  g, DoD = 13.6 m/s). Both classify as ICAO Moderate. The lower DoD reflects the reduced oscillation amplitude in the area model. Longitudinal and transverse loads ( $n_x, n_y$ ) are negligible in both models for Case 1.

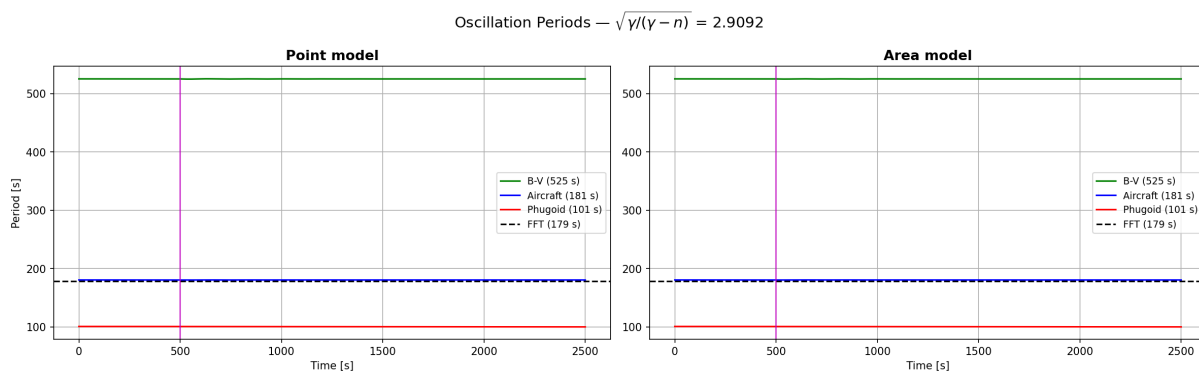


Figure 5: Characteristic oscillation periods: point model (left) vs. area model (right). Both show B-V period (526 s), aircraft oscillation period (181 s), phugoid period (101 s), and the FFT-observed period ( $\sim 179$  s). The ratio  $\sqrt{\gamma/(\gamma - n)} = 2.909$  is altitude-independent and identical in both models.

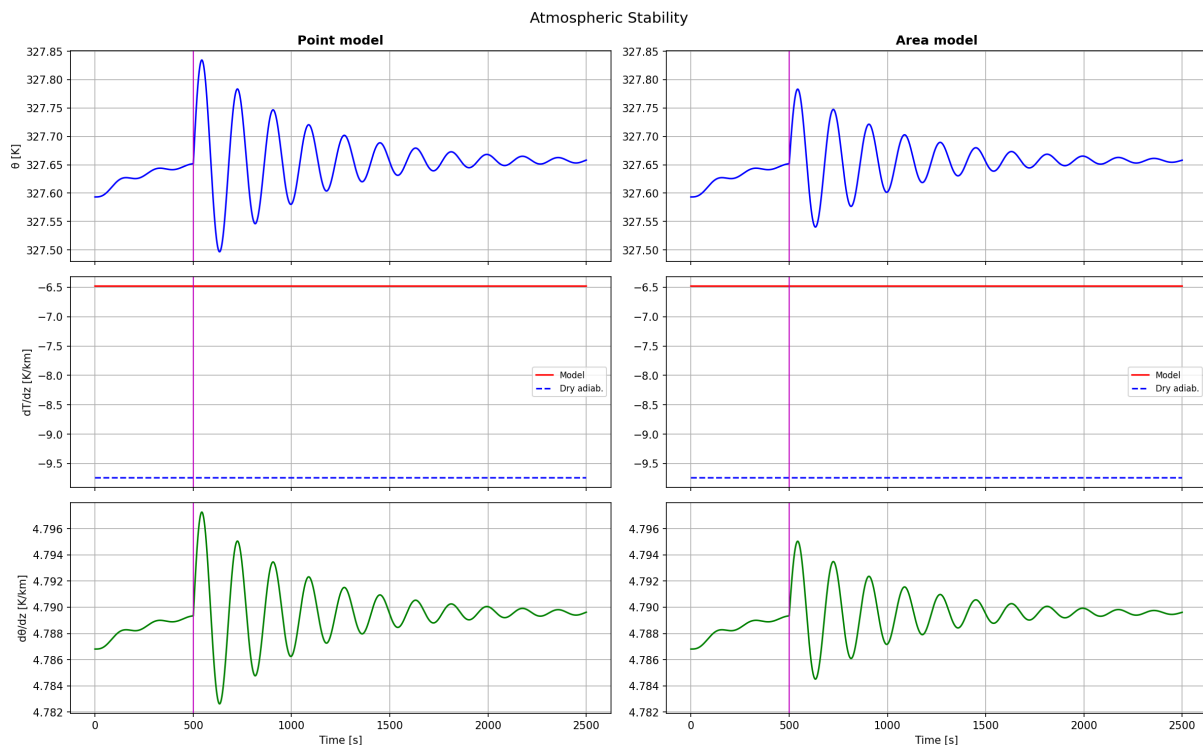


Figure 6: Atmospheric stability: point model (left) vs. area model (right). Potential temperature  $\theta$ , model vs. dry adiabatic lapse rate, and  $d\theta/dz$  are identical in both models since they depend only on altitude, not on the aircraft model.

stability) are model-independent. They oscillate with altitude as the aircraft bobs up and down, but the amplitude of the atmospheric oscillation differs because the altitude excursion differs.

### 3.2.4 Energy Budget

Figures 7 and 8 show the energy budget. The VT deposits a larger energy impulse in the point model because the peak acceleration is higher. In both cases, the VT energy is subsequently dissipated by aerodynamic damping over the post-encounter oscillation. The energy conservation error (bottom panel of Figure 8) remains below 0.01% of the total energy, validating the RK4 time integration.

### 3.2.5 Spectral Analysis and Aeroacoustics

Figure 9 shows the Hanning-windowed FFT periodogram of the altitude signal  $z(t)$ . The spectral peak is at  $f \approx 0.0056$  Hz ( $T \approx 179$  s) in both models, matching the analytical prediction (181 s) to within 1.5%. The point model has  $\sim 3\times$  higher PSD at the peak, consistent with the 33% larger oscillation amplitude (PSD scales as amplitude squared).

Figures 10–12 present the aeroacoustic analysis. The signed acoustic pressure  $p'(t)$  from Eq. (40) shows a sharper impulse in the point model because the acceleration onset is instantaneous (step function) rather than ramped (the area model's gradual wing immersion). The STFT spectrograms (Figure 11) reveal identical three-phase structure in both models: (1) a broadband vertical stripe during the VT transit, (2) narrowband energy concentration at  $\sim 0.006$  Hz, and (3) exponential decay with time constant  $\tau = 252$  s. All acoustic energy lies below the human hearing threshold of 20 Hz. Only the brief VT impulse ( $< 1$  s) exceeds the infrasound perception threshold of  $\sim 94$  dB at 5 Hz.

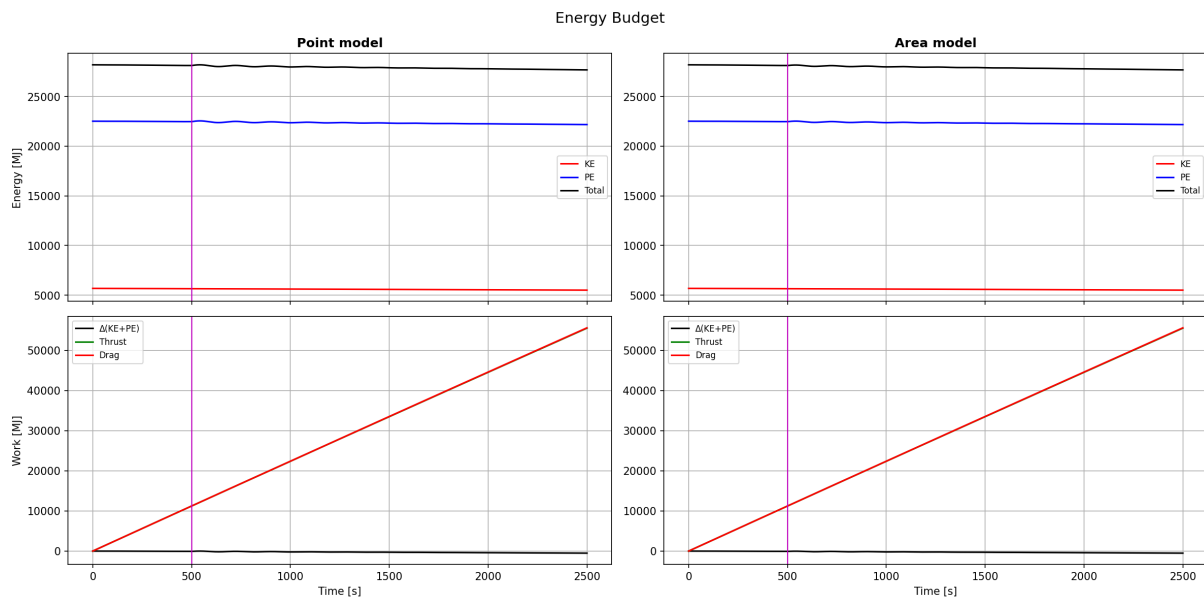


Figure 7: Energy budget: point model (left) vs. area model (right). Top: kinetic, potential, and total energy. Bottom: cumulative drag, damping, and thrust work. The VT deposits less energy into the oscillation in the area model, but the thrust and drag work (dominated by steady cruise) are identical.

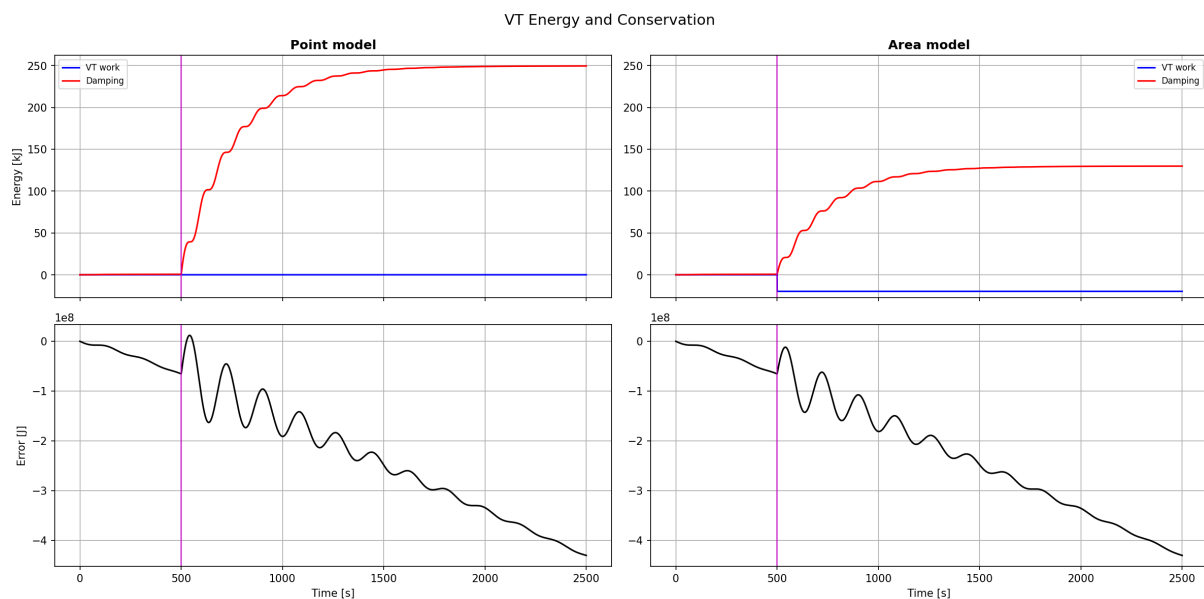


Figure 8: VT energy input and conservation: point model (left) vs. area model (right). The VT work is delivered as a single impulse. The energy conservation error is bounded at  $< 0.01\%$  of total energy in both models, validating the RK4 integration.

### 3.2.6 Flight Dynamics and Fuel

Figures 13 and 14 show the flight dynamics and fuel consumption. The flight path angle oscillates with larger amplitude in the point model ( $\sim 0.4^\circ$  vs.  $\sim 0.3^\circ$ ), consistent with the larger vertical velocity perturbation. Fuel consumption is identical in both models because the TSFC-based fuel burn depends on thrust, which is determined by the cruise equilibrium rather than the oscillation. The slight decrease in burn rate over time reflects the reducing aircraft mass ( $m/m_{\text{init}}$  correction in the thrust model).

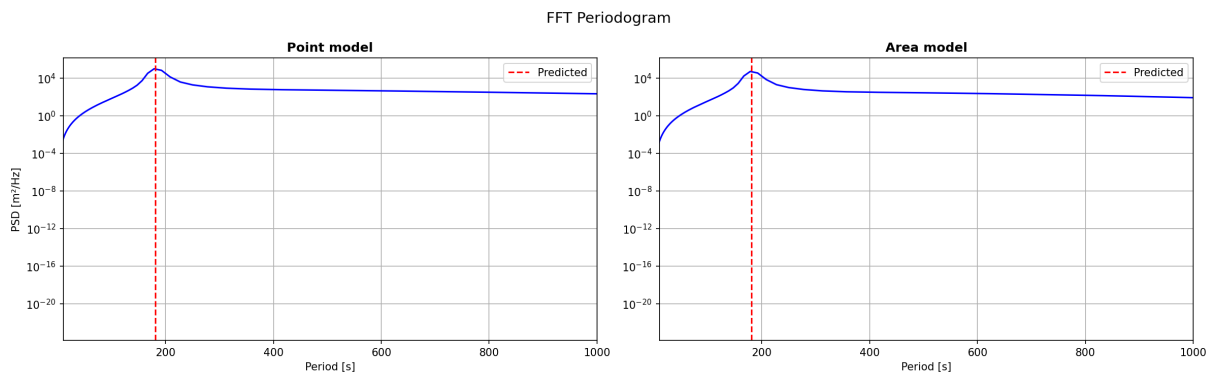


Figure 9: FFT periodogram of  $z(t)$ : point model (left) vs. area model (right). Both show a sharp spectral peak at the aircraft oscillation frequency. The point model has higher PSD (larger oscillation amplitude) but the peak frequency is identical.

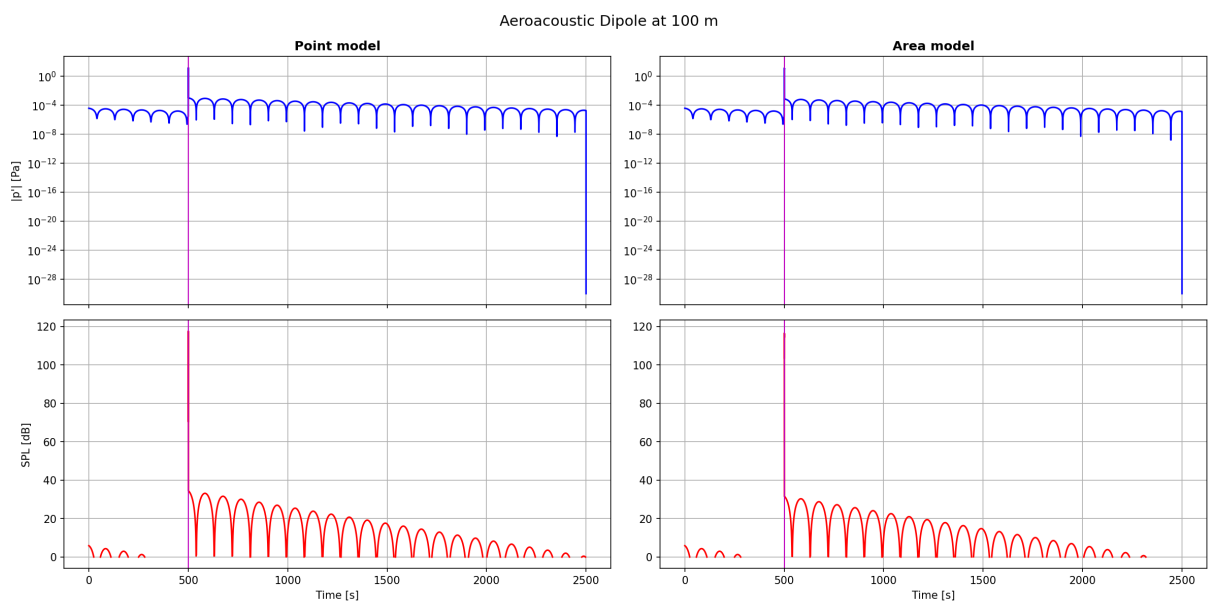


Figure 10: Acoustic pressure and SPL at 100 m: point model (left) vs. area model (right). The point model produces a sharper impulse ( $\sim 120$  dB peak) because  $da/dt$  is larger for the instantaneous acceleration onset. The post-encounter SPL oscillation (25–35 dB) is model-independent in character but lower in amplitude for the area model.

### 3.2.7 Sound Generation

Figure 15 shows the trajectory-based vorticity estimates and the Howe sound source term  $S = (1/\rho)\nabla \cdot (\rho\boldsymbol{\omega} \times \mathbf{v})$  [19]. For Case 1, only  $|\omega_y|$  is physically significant because the VT vorticity is purely in the  $y$ -direction ( $\phi = \theta = \pi/2$ ). The  $|\omega_x|$  and  $|\omega_z|$  panels are empty (values below the physical threshold). The area model shows lower vorticity magnitudes, consistent with the reduced acceleration perturbation.

### 3.2.8 Area Fractions (Area Model Only)

Figure 16 shows the area fractions that modulate the vortex-induced acceleration in the area model. The peak wing fraction of  $\sim 0.87$  means the VT covers 87% of the wing area at closest approach. The fuselage fraction reaches  $\sim 1.0$  briefly (the fuselage cross-section is smaller than the VT). Left and right wing fractions are equal (symmetric encounter), and forward and aft

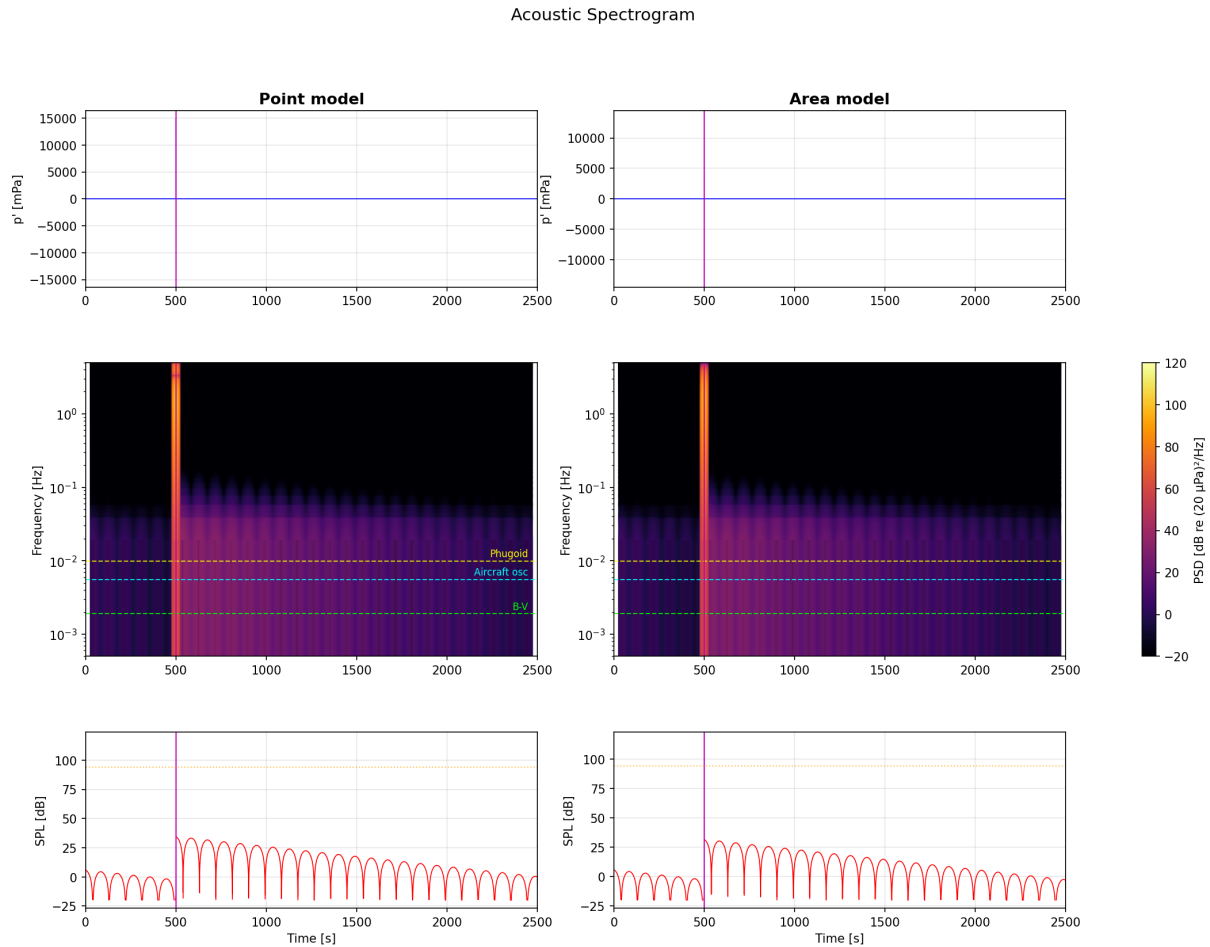


Figure 11: Acoustic spectrogram: point model (left) vs. area model (right). Both show the three-phase pattern: broadband impulse at  $t \approx 500$  s, narrowband relaxation at the aircraft oscillation frequency, and exponential decay. The impulse is slightly more broadband in the point model due to the sharper acceleration onset. All energy lies below the 20 Hz hearing threshold.

fuselage fractions overlap. For asymmetric VT orientations (Cases 4–17), these fractions would differ, producing differential forces and potentially roll or yaw perturbations.

## 4 Discussion

### 4.1 Comparison with Previous Work

The Python RK4 implementation produces oscillation periods within 1.5% of the analytical prediction, compared to  $\sim 3\%$  discrepancy in the original MATLAB forward Euler code. The elimination of the stabilisation phase removes the artificial pre-VT oscillations visible in the original results and reduces the total simulation time by  $\sim 50\%$ . The analytical cylinder test eliminates the 0.7% volume error of the Delaunay hull approach.

The key physics insight—that the post-VT oscillation frequency is  $\sqrt{\gamma/(\gamma - n)}$  times the B-V frequency—was not available in the original work, where it was obtained by empirical fitting (2.893 vs. the analytical 2.909).

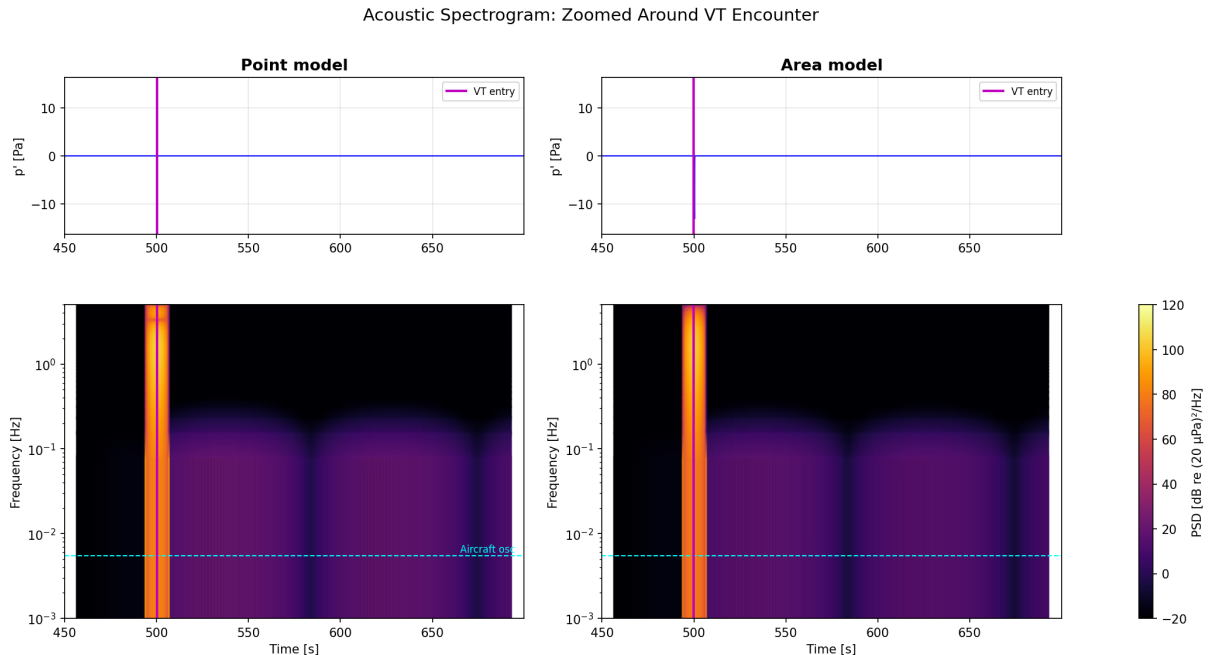


Figure 12: Zoomed acoustic spectrogram around the VT encounter: point model (left) vs. area model (right). The broadband-to-narrowband transition takes 1–2 oscillation cycles in both models.

## 4.2 Analogy with Edge-Localised Modes in Fusion Plasmas

The spectrogram structure of the VT encounter bears a striking resemblance to that of edge-localised modes (ELMs) in fusion plasmas. ELMs are magnetohydrodynamic (MHD) instabilities that occur in the high-confinement mode (H-mode) edge transport barrier of fusion plasmas [21, 22]. Each ELM “crash” expels particles and energy from the confined plasma, analogous to the VT depositing energy into the aircraft’s oscillatory motion. The first H-mode was observed in the ASDEX tokamak [23].

Recent work by García-Muñoz et al. [24] presents ELM-synchronised spectrograms of radial magnetic field fluctuations measured by Mirnov coils. These show a three-phase structure mapping directly onto the VT encounter:

Phase	ELM crash (fusion plasmas)	VT encounter (aircraft)
1. Impulse	Broadband to $\sim 300$ kHz, $\sim 0.1$ – $1$ ms	Broadband to $\sim 3$ Hz, $\sim 0.2$ s
2. Relaxation	Narrowband $f < 50$ kHz, $\sim 3$ ms	Narrowband at $0.006$ Hz, $\sim 1000$ s
3. Restoring	Pressure gradient rebuilds pedestal	Lift-density coupling restores altitude

The timescales differ by  $\sim 10^5$ – $10^7$ , but the spectrogram topology is identical: broadband impulse  $\rightarrow$  narrowband relaxation  $\rightarrow$  exponential damping. Both systems have a *pressure or density gradient* that provides the restoring force: the steep pedestal pressure gradient for ELMs [22], and the atmospheric density gradient for the aircraft (Eq. 35).

### 4.2.1 Mathematical Structure: Vortex Force Analogy

The analogy extends beyond spectrogram topology to the mathematical structure of the perturbation. In the VT model, the acceleration per unit mass is given by the vortex acceleration (Eq. 1):

$$\mathbf{a}_{\text{VT}} = \frac{1}{2}\boldsymbol{\omega} \times \mathbf{v}, \quad (42)$$

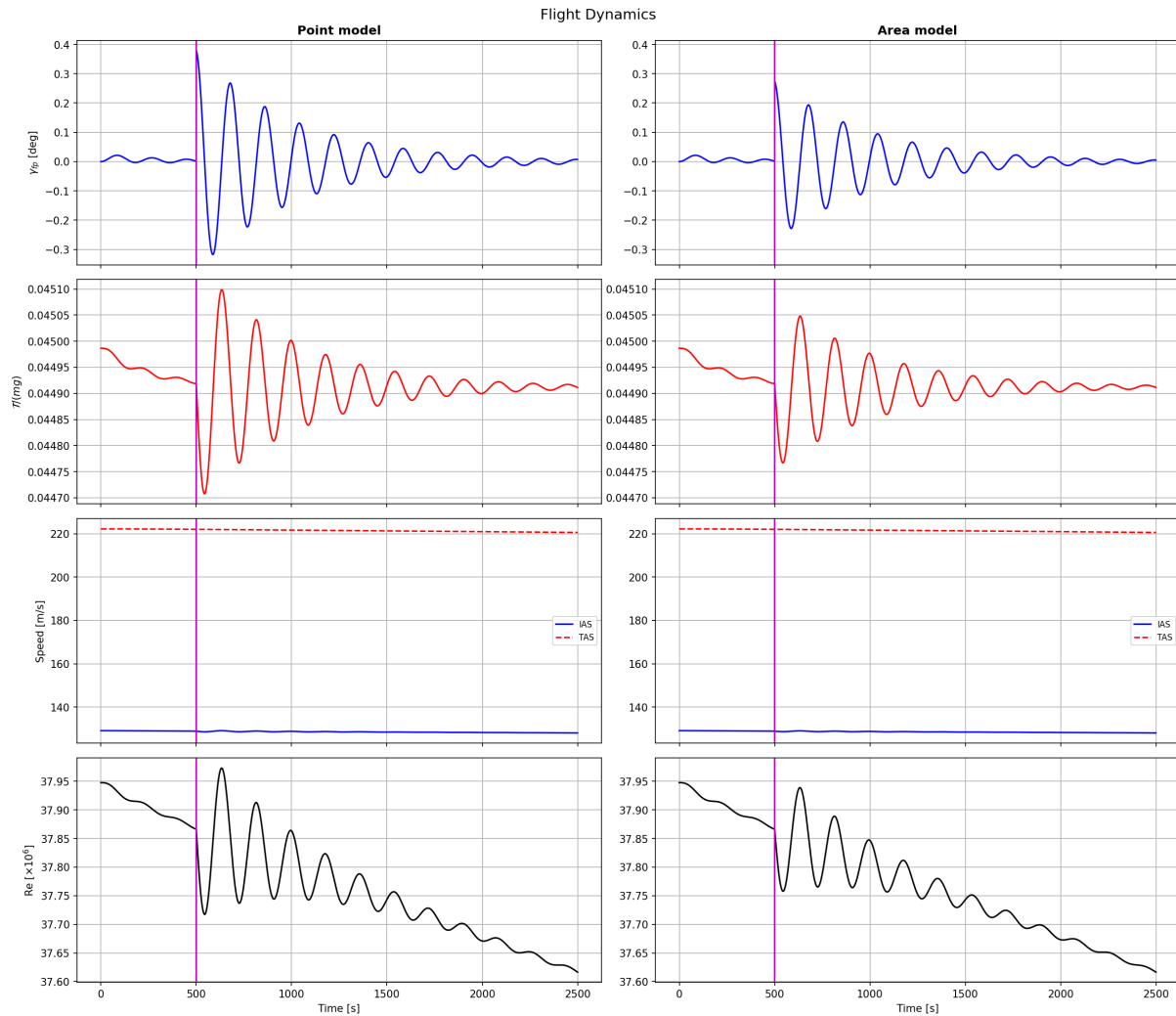


Figure 13: Flight dynamics: point model (left) vs. area model (right). Flight path angle, thrust-to-weight ratio, indicated airspeed (IAS) vs. true airspeed (TAS), and Re. The flight path angle oscillation is larger in the point model ( $\sim 0.4^\circ$  vs.  $\sim 0.3^\circ$ ); all other quantities are model-independent.

where  $\boldsymbol{\omega} = \nabla \times \mathbf{v}_{VT}$  is the fluid vorticity. In MHD, the corresponding force on the plasma is the Lorentz force:

$$\mathbf{F}_{\text{MHD}}/\rho = \mathbf{j} \times \mathbf{B}/\rho, \quad (43)$$

where  $\mathbf{j} = \nabla \times \mathbf{B}/\mu_0$  is the current density—essentially the “magnetic vorticity”. Both expressions have the structure of a vector cross product between a curl quantity ( $\boldsymbol{\omega}$  or  $\mathbf{j}$ ) and a field ( $\mathbf{v}$  or  $\mathbf{B}$ ), and both vanish in the unperturbed equilibrium.

ELM filaments are helical vortical structures carrying both fluid vorticity ( $\nabla \times \mathbf{v}$ ) and current ( $\nabla \times \mathbf{B}$ ). The peeling component of the peeling-ballooning instability is specifically current-driven, analogous to how the VT encounter is vorticity-driven. The proper mapping between the two systems is:

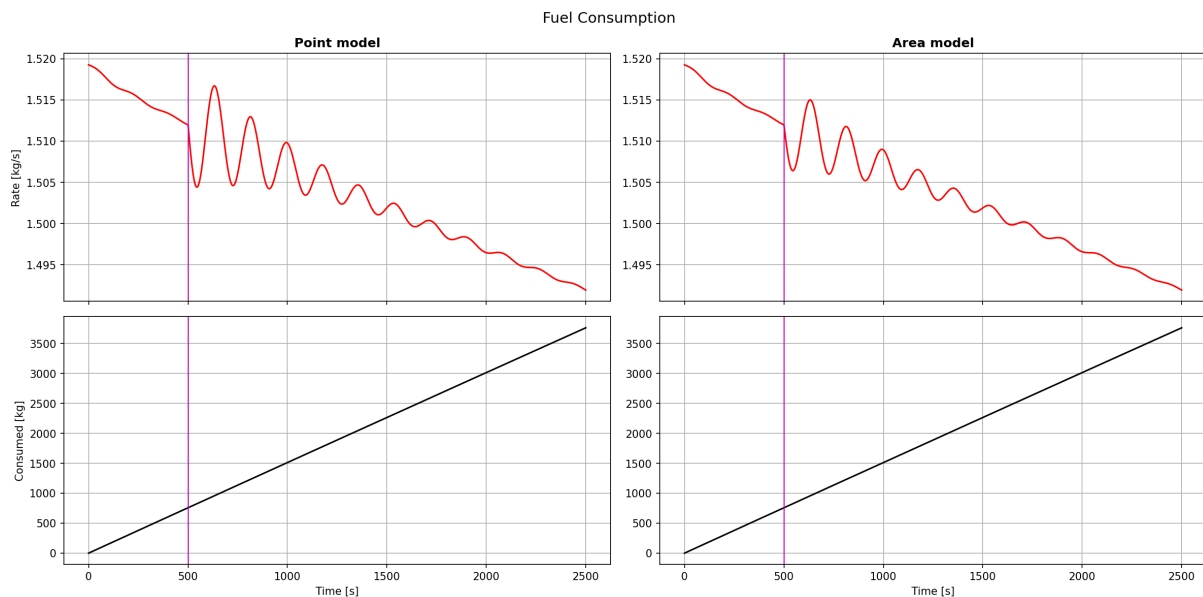


Figure 14: Fuel consumption: point model (left) vs. area model (right). The instantaneous burn rate ( $\sim 1.5$  kg/s) and cumulative consumption (3761 kg over 2500 s) are identical, confirming that the fuel model depends on thrust (which is set by the cruise condition), not on the oscillation amplitude.

VT-Aircraft	Fusion plasma ELM
Atmosphere (density gradient)	Plasma edge (pressure gradient)
Aircraft (equilibrium structure)	Pedestal (equilibrium structure)
VT vorticity $\boldsymbol{\omega}$	MHD mode (current $\mathbf{j}$ , flow)
Vortex acceleration $\frac{1}{2}\boldsymbol{\omega} \times \mathbf{v}$	Lorentz acceleration $\mathbf{j} \times \mathbf{B}/\rho$
Lift-density restoring mechanism	Pressure gradient restoring mechanism
Aerodynamic damping	Turbulent transport

The aircraft is not the plasma—the aircraft is more analogous to the *pedestal*: a structure held in equilibrium by a gradient, displaced by a vortical perturbation, then oscillating back. The VT and the ELM are both vortical perturbations that deposit energy impulsively.

#### 4.2.2 ELM Types and VT Encounter Patterns

ELMs are classified into types based on their frequency, amplitude, and relation to the MHD stability boundary [21, 22]:

- **Type I** ELMs are large, isolated crashes with regular periodicity, occurring when the edge pressure gradient exceeds the peeling-ballooning stability limit. They correspond to *single, well-separated* VT encounters.
- **Type II** ELMs are smaller, more frequent events observed in strongly shaped plasmas. These may correspond to encounters with *clusters or trains* of smaller VTs.
- **Type III** ELMs are small, high-frequency, irregular events appearing at lower heating power. Their irregular character is reminiscent of aircraft encounters with *scattered, disorganised vorticity*—such as CAT with no dominant coherent structure.

Additionally, *dithering* between H-mode and L-mode (low-confinement mode) produces rapid, irregular bursts [21]. This is analogous to an aircraft passing through *bunches of VTs* at irregular intervals. The code’s multi-VT capability can model all of these patterns.

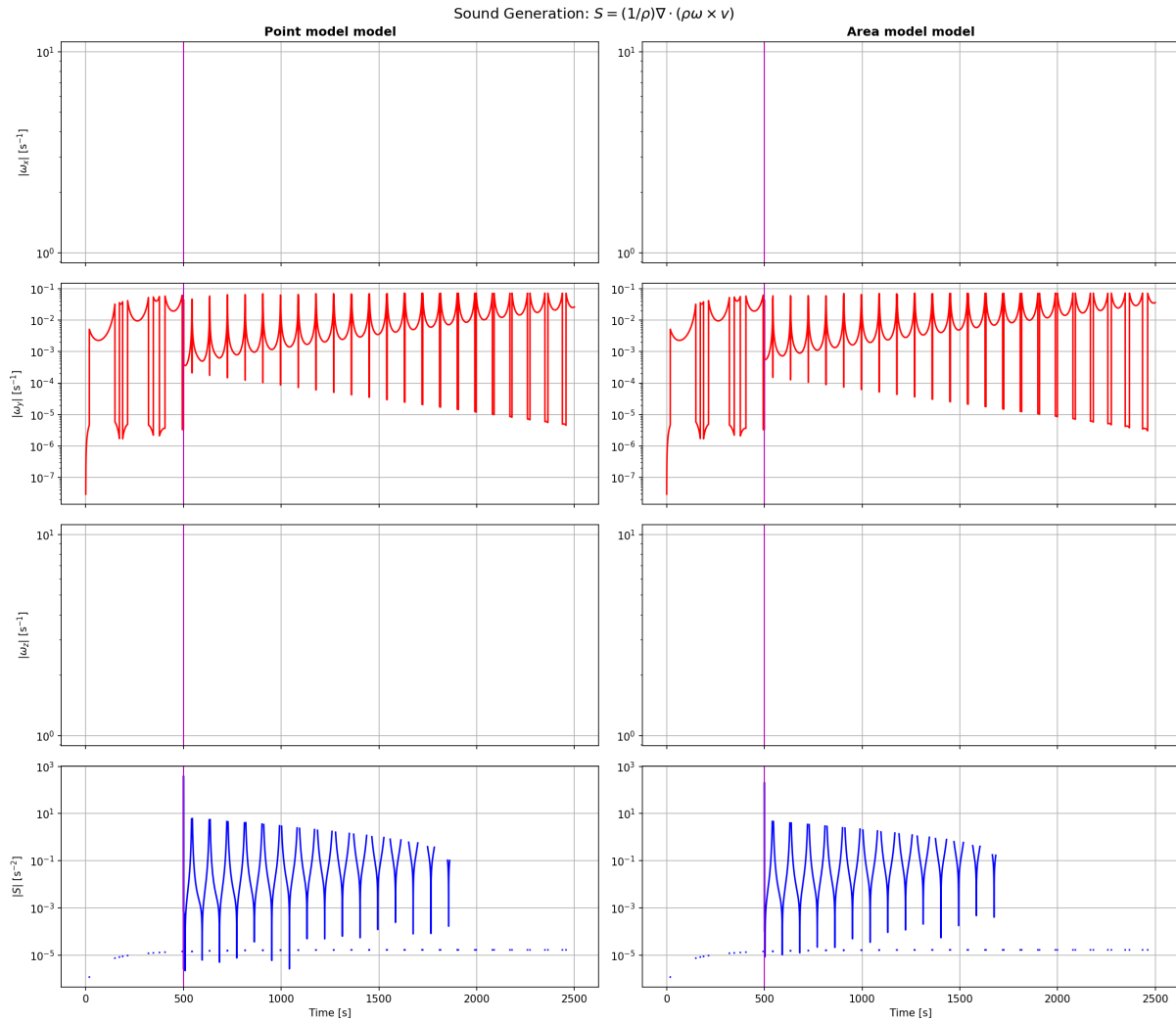


Figure 15: Sound generation: point model (left) vs. area model (right). Aircraft vorticity components  $|\omega_x|$ ,  $|\omega_y|$ ,  $|\omega_z|$  and Howe source term  $|S|$ . Only  $|\omega_y|$  is non-zero for Case 1 ( $\phi = \theta = \pi/2$ ). The area model shows slightly lower vorticity magnitudes, consistent with the reduced accelerations.

### 4.2.3 Key Differences

ELMs are *internally driven*: the plasma becomes unstable when the edge gradient exceeds a threshold, producing a self-limiting crash-and-recovery cycle. The VT encounter is *externally driven*: an external vortex hits the aircraft in stable equilibrium. ELMs cycle periodically; the VT event is a one-shot perturbation (unless multiple VTs are encountered).

### 4.3 Model Limitations

1. **Fixed angle of attack:** The default model uses constant  $C_d$  and  $C_l$ . A real aircraft adjusts AoA continuously. The optional drag polar mode addresses this but represents an idealised autopilot.
2. **No wind:** The atmosphere is quiescent. A background wind profile would modify both the VT formation conditions and the aircraft response.
3. **Simplified drag:** Using  $v_x^2$  instead of  $|\mathbf{v}|^2$  in the drag formula is valid for small perturbations but would become inaccurate for severe events.

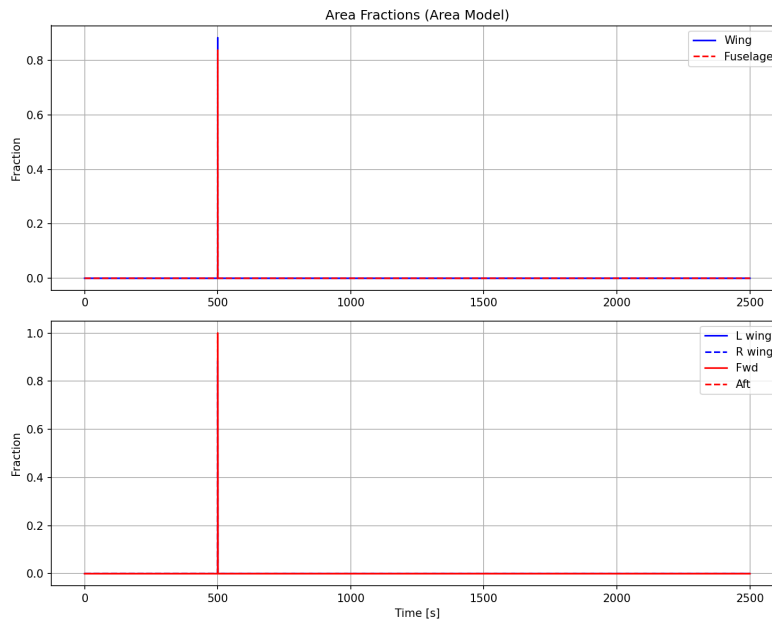


Figure 16: Wing and fuselage area fractions inside the VT (area model only). Top: total wing and fuselage fractions. Bottom: left/right wing and forward/aft fuselage decomposition. The peak wing fraction ( $\sim 0.87$ ) is less than unity because the VT width ( $W = 53.2$  m) does not fully cover the wing span ( $S = 60$  m). The symmetric Case 1 produces equal left and right wing fractions.

4. **Solid-body rotation:** The VT has uniform vorticity with uniform vorticity throughout the cylinder. Real atmospheric vortices have more complex radial profiles (e.g., Rankine or Lamb–Oseen).
5. **No structural flexibility:** The aircraft is treated as a rigid point mass (or rigid cross-sections in the area model). Structural modes (wing bending, fuselage flex) are not modelled.

#### 4.4 Future Research Directions

1. **Flight data comparison:** Validate the model against flight data recorder (FDR) measurements using  $\Delta n$  and acceleration spectra as comparison metrics. The g-load output is directly comparable to FDR data.
2. **Multiple vortex tubes:** The code supports co- and counter-rotating VT pairs, but the parameter space (separation distance, relative strength, orientation) has not been systematically explored. Wake vortex encounters from preceding aircraft are a natural application.
3. **Realistic flight control:** A pitch-hold or altitude-hold autopilot with finite bandwidth would modify the damping and frequency. The current variable-AoA mode is an idealised limit.
4. **Non-polytropic atmospheres:** Real atmospheric profiles with temperature inversions, tropopause, or jet streams would modify both the oscillation frequency and VT formation conditions.
5. **Drone-specific studies:** Systematic parameter studies for small UAS encountering atmospheric VTs, using the `small_drone()` preset.

6. **Acoustic signatures:** Compare the aeroacoustic dipole SPL estimates with microphone measurements during turbulence events. The infrasound component ( $f \sim 0.006$  Hz) may be detectable with dedicated instruments.
7. **Radial vorticity profiles:** Replace solid-body rotation with Rankine or Lamb–Oseen profiles for more realistic VT encounters.
8. **ELM analogy:** Investigate whether ELM control techniques (resonant magnetic perturbations [24], pellet injection) have analogues in aviation turbulence mitigation, and whether the stability diagram framework used for ELM classification [22] can be adapted for VT encounter severity prediction.
9. **Turbulence spectra:** Superimpose broadband turbulence on the VT encounter to assess how coherent vortex structures interact with the turbulence background.

## 5 Conclusions

A modular Python simulation of aircraft motion during vortex tube encounters has been developed, replacing and extending the original MATLAB implementation of Basse [7, 18]. The key contributions are:

1. **Physics-derived constants:** The B-V calibration ratio  $\sqrt{\gamma/(\gamma - n)} = 2.909$  is derived analytically from the polytropic model, replacing the empirically fitted value of 2.893. The polytropic index  $n$  is itself derived from the ISA lapse rate via Eq. (4).
2. **Aircraft oscillation frequency:** The dominant post-VT oscillation period ( $\sim 181$  s at 10 km) is identified as a lift-density coupling mode, Eq. (35), distinct from both the Brunt–Väisälä frequency (526 s) and the phugoid frequency (101 s). The ratio  $\omega_{\text{aircraft}}/N_{\text{BV}}$  is altitude-independent.
3. **Self-consistent modelling:** Damping ( $c_1 = \rho v C_d A$ ), fuel consumption (TSFC model), and all atmospheric quantities are derived from fundamental parameters without free fitting constants.
4. **Numerical improvements:** RK4 integration with single-phase analytical trim, analytical cylinder test, bounding-box pre-check, and multi-VT support.
5. **Comprehensive diagnostics:** 26 plots covering dynamics, atmospheric stability, energy budgets, turbulence severity classification (ICAO  $\Delta n$  bands), passenger comfort (Dose of Discomfort), flight dynamics (IAS, flight path angle, Reynolds number), and aeroacoustic analysis (dipole SPL).

The code is freely available as a Python package requiring only NumPy, SciPy, and Matplotlib. It runs from Spyder (press F5) or the command line, and supports 19 predefined VT configurations.

## A Code Structure

The package consists of 11 files totalling  $\sim 2800$  lines of Python. Table 3 provides an overview.

Table 3: Files in the VT-Aircraft package.

File	Purpose	Lines
atmosphere.py	Polytropic atmosphere model (Section 2.1)	251
vehicle.py	Vehicle configuration and presets (Section 2.3)	136
vortex_tube.py	VT geometry, intersection tests (Section 2.2)	315
simulation.py	RK4 engine, multi-VT, drag polar (Section 2.4)	510
postprocessing.py	All derived quantities (Appendix E)	459
plotting.py	26 matplotlib figure functions (Appendix F)	750
cases.py	19 predefined VT configurations (Appendix D)	112
run_spyder.py	Spyder/interactive runner (Appendix C)	134
run_simulation.py	Command-line interface (CLI)	234
__init__.py	Package metadata	25
README.md	User documentation	—

## A.1 Algorithm and Dataflow

Figure 17 shows the complete dataflow from configuration inputs to output plots. The pipeline consists of five stages: configuration, atmosphere/trim initialisation, RK4 time integration, post-processing, and plotting.

### A.1.1 Algorithmic Description

The simulation algorithm is given in pseudocode below.

Listing 1: Main simulation algorithm.

```

1 INITIALISE:
2   Load VehicleConfig, VortexTubeConfig, SimulationConfig
3   Compute atmosphere: n from ISA, g(z), rho(z), T(z)
4   Compute trim: Cd = 2*T_init/(rho*v^2*A), Cl = 2*mg/(rho*v^2*A)
5   Compute damping: c1 = rho*v*Cd*A (aero mode)
6   Compute VT: R, W, Omega, omega(phi, theta)
7   Set state: s = [x0, 0, z0, v0, 0, 0], m = m_init
8
9 TIME INTEGRATION (RK4):
10  for k = 0 to n_steps-1:
11    Evaluate atmosphere at current z:
12      g_k, rho_k, T_k = atmosphere(z_k)
13
14    Define derivatives F(s):
15      ax = T/m - Cd*rho*A*vx^2/(2m)
16      ay = -c1*vy/m
17      az = Cl*rho*A*vx^2/(2m) - g - c1*vz/m
18
19    if point_inside_VT(x, y, z): [or area_fractions]
20      ax += 0.5*(wy*vz - wz*vy) * [fw if area model]
21      ay += 0.5*(wz*vx - wx*vz) * [ff if area model]
22      az += 0.5*(wx*vy - wy*vx) * [fw if area model]
23
24    if multi_VT:
25      sum contributions from each VT
26
27    return [vx, vy, vz, ax, ay, az]
28
29 RK4 sub-steps:
30  k1 = F(s_k)
31  k2 = F(s_k + dt/2 * k1)

```

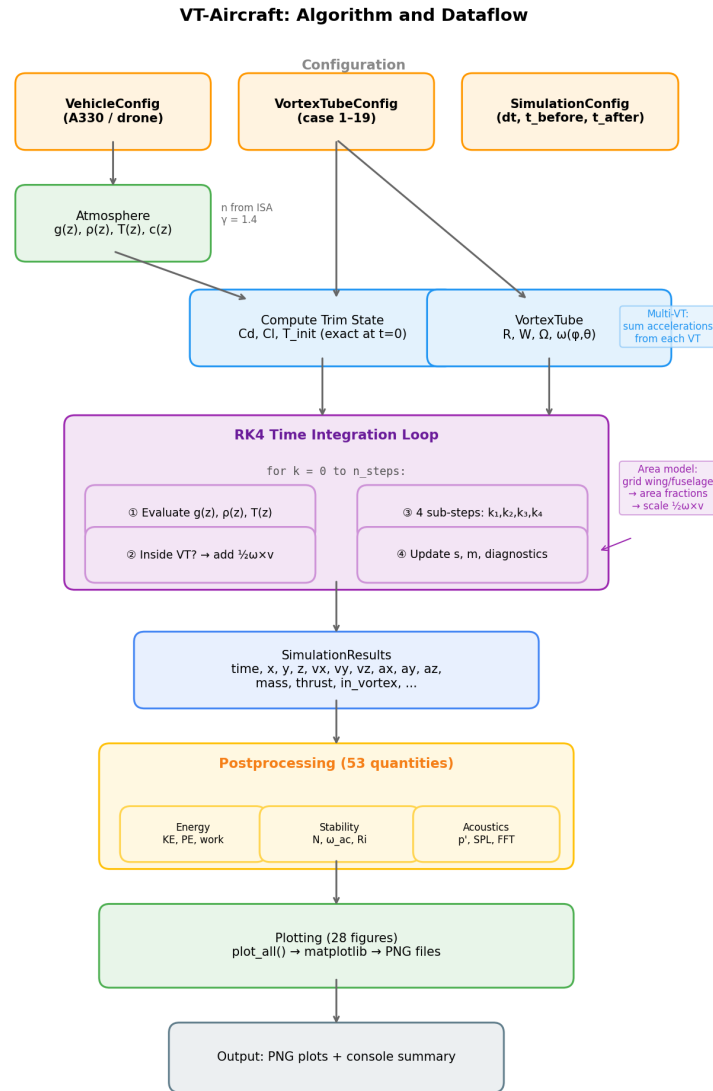


Figure 17: Algorithm and dataflow of the VT-Aircraft simulation. Orange: configuration inputs. Green: atmosphere model. Blue: initialisation. Purple: RK4 integration loop (the computational core). Yellow: postprocessing (53 derived quantities). The area model and multi-VT extensions are shown as annotations.

```

32 |         k3 = F(s_k + dt/2 * k2)
33 |         k4 = F(s_k + dt * k3)
34 |         s_{k+1} = s_k + dt/6 * (k1 + 2*k2 + 2*k3 + k4)
35 |
36 |     Update mass: m_{k+1} = m_k - TSFC * T_k * dt
37 |     Store diagnostics: time, state, accelerations, mass
38 |
  
```

```

39 POSTPROCESS:
40   Compute 53 derived quantities from time series
41   (energy, stability, g-loads, acoustics, FFT, ...)
42
43 PLOT:
44   Generate 28 diagnostic figures via plot_all()

```

The computational cost is dominated by the RK4 loop. For the default configuration (25 000 steps, point model), the loop completes in  $\sim 0.3$  s on a modern laptop. The area model is slower ( $\sim 2.2$  s) due to the grid intersection test at each step, mitigated by a bounding-box pre-check that provides a  $2.7\times$  speedup. Postprocessing and plotting add  $\sim 1$  s each.

## A.2 Key Classes

**PhysicalConstants** (dataclass in `atmosphere.py`): Stores fundamental constants ( $G$ ,  $m_{\text{Earth}}$ ,  $r_{\text{Earth}}$ ,  $\rho_0$ ,  $p_0$ ,  $T_0$ ,  $\gamma$ ,  $R_{\text{air}}$ , ISA lapse rate). The polytropic index  $n$ ,  $R/c_p$ , and  $c_p$  are `@property` methods derived from the stored fields.

**Atmosphere** (class in `atmosphere.py`): Provides all atmospheric computations. Key methods: `gravity(z)`, `density(g, z)`, `temperature(g, z)`, `pressure(rho, T)`, `dynamic_viscosity(T, rho)`, `speed_of_sound(p, rho)`, `potential_temperature(T, p)`, `brunt_vaisala_frequency(g, z)`, `aircraft_oscillation_frequency(g, z)`, `bv_to_aircraft_ratio()`.

**VehicleConfig** (dataclass in `vehicle.py`): Stores all aircraft parameters. Key fields: geometry (`wing_chord`, `wing_span`, `fuselage_length`, `fuselage_height`), mass/fuel (`mass_initial`, `tsfc`), thrust (`thrust_sea_level`, `thrust_factor`), initial conditions (`altitude_initial`, `speed_initial`), damping (`c1_y`, `c1_z`), drag polar (`use_drag_polar`, `oswald_efficiency`). Methods: `compute_damping_aero(rho, Cd)`, `compute_damping_from_vt(g)`.

**VortexTube** (class in `vortex_tube.py`): Computes VT geometry from `VortexTubeConfig`. Key methods: `position_at(y, z, x)`, `point_inside(x, y, z)`, `area_fractions(x_le, y, z)`, `vortex_acceleration(vx, vy, vz, fw, ff)`.

**Simulation** (class in `simulation.py`): Main runner. Constructor accepts single `VortexTubeConfig` or a list for multiple VTs. Key methods: `_compute_trim_state()`, `_derivatives(state, ...)`, `_rk4_step(state, ...)`, `run()`.

## B Dependencies and Installation

**Requirements:** Python 3.8+, NumPy, SciPy, Matplotlib.

```
pip install numpy scipy matplotlib
```

Place all `.py` files in a single directory. Run in Spyder (open `run_spyder.py`, press F5) or from the command line:

```
python run_simulation.py --case 1 --save-dir output
python run_simulation.py --case 1 --no-fuel --t-before 200 --t-after 3000
python run_simulation.py --case 1 --model area --damping strong
python run_simulation.py --list-cases
```

Programmatic usage:

```

1 from run_simulation import run_case
2 results, pp = run_case(case=1, t_before=500, t_after=3000,
3                       damping='aero')
4 print(pp.dominant_period, pp.peak_incremental_load)

```

## C Configuration Reference

Table 4: Configuration parameters in `run_spyder.py`.

Parameter	Default	Description
CASE	1	Predefined case number (1–19)
MODEL	'point'	Aircraft model: 'point' or 'area'
DAMPING	'aero'	Damping: 'none', 'aero', 'strong', or numeric [kg/s]
TSFC	$15 \times 10^{-6}$	Thrust-specific fuel consumption [kg/(N·s)]
T_BEFORE	500	Flight time before VT encounter [s]
T_AFTER	2000	Flight time after VT encounter [s]
DT	0.1	Time step [s]
USE_DRAG_POLAR	False	Variable-AoA autopilot with drag polar
OSWALD_EFFICIENCY	0.8	Oswald span efficiency (if polar enabled)
MULTI_VT	None	List of <code>VortexTubeConfig</code> for multiple VTs
ACOUSTIC_OBSERVER_DISTANCE	100	Observer distance for SPL calculation [m]

## D Predefined Cases

Nineteen predefined VT configurations are provided. Cases 1–17 correspond to those in Basse [7]; Cases 18–19 are from the draft paper [18].

Table 5: Predefined VT cases. All cases use  $a_g = 0.5$  unless noted.

Case	Description	$r_A$	$\phi$	$\theta$	Offsets
1	Large VT, transverse horiz.	10	$\pi/2$	$\pi/2$	—
2	Small VT, transverse horiz.	0.1	$\pi/2$	$\pi/2$	—
3	Baseline VT	1	$\pi/2$	$\pi/2$	—
4	Baseline + horiz. offset	1	$\pi/2$	$\pi/2$	$y_0 = W/2$
5	Baseline + vert. offset	1	$\pi/2$	$\pi/2$	$z_0 = R\sqrt{3/4}$
6	$\phi$ variation	1	$\pi/4$	$\pi/2$	—
7	$\phi$ variation	1	$3\pi/4$	$\pi/2$	—
8	$\theta$ variation	1	$\pi/2$	$\pi/4$	—
9	$\theta$ variation	1	$\pi/2$	$3\pi/4$	—
10–13	Combined $\phi/\theta$ variations	1	varies		—
14	VT parallel to aircraft	1	0	$\pi/2$	—
15	VT anti-parallel	1	$\pi$	$\pi/2$	—
16	Columnar vortex	1	$\pi/2$	0	—
17	Columnar anti-parallel	1	$\pi/2$	$\pi$	—
18	Large vertical VT (EOM case)	10	$\pi/2$	$\pi$	—
19	Large longitudinal VT (EOM case)	10	$\pi$	$\pi/2$	—

## E Postprocessing Quantities

The `postprocess()` function in `postprocessing.py` computes 53 derived quantities from the simulation time series. These are stored in the `PostprocessingResults` dataclass. Table 6 groups them by category.

Table 6: Postprocessing quantities computed by `postprocess()`.

Quantity	Formula / definition	Unit
<i>Energy</i>		
$E_{\text{kin}}$	$\frac{1}{2}m(v_x^2 + v_y^2 + v_z^2)$	J
$E_{\text{pot}}$	$mgz$	J
$E_{\text{total}}$	$E_{\text{kin}} + E_{\text{pot}}$	J
$E_{\text{drag,x}}$	$-\int C_d \rho A v_x^3 / 2 dt$	J
$E_{\text{drag,y}}$	$-\int c_1 v_y^2 dt$	J
$E_{\text{drag,z}}$	$-\int c_1 v_z^2 dt$	J
$E_{\text{thrust}}$	$\int \mathcal{T} v_x dt$	J
$E_{\text{VT}}$	$\int m(\mathbf{a}_{\text{VT}} \cdot \mathbf{v}) dt$	J
$E_{\text{error}}$	Conservation check	J
<i>Speed of sound and Mach</i>		
$c$	$\sqrt{\gamma p / \rho}$	m/s
$M$	$ \mathbf{v}  / c$	—
$ \mathbf{v} $	$\sqrt{v_x^2 + v_y^2 + v_z^2}$	m/s
<i>Atmospheric stability</i>		
$\theta$	$T(p_0/p)^{R/c_p}$	K
$N$	$\sqrt{(g/\theta)(d\theta/dz)}$ , analytical	rad/s
$\omega_{\text{aircraft}}$	$\sqrt{-g/\rho \cdot d\rho/dz}$ , Eq. (35)	rad/s
$\omega_{\text{ac}}/N$	$\sqrt{\gamma/(\gamma - n)}$	—
$\Gamma$	$dT/dz$ , lapse rate	K/m
$\Gamma_{\text{dry}}$	$-g/c_p$	K/m
$d\theta/dz$	Analytical from polytropic model	K/m
<i>Richardson number</i>		
$v_{\text{hor}}$	$\sqrt{v_x^2 + v_y^2}$	m/s
$dv_{\text{hor}}/dz$	Vertical shear	$\text{s}^{-1}$
$Ri$	$\omega_{\text{aircraft}}^2 / (dv_{\text{hor}}/dz)^2$ (cf. [25])	—
<i>Phugoid</i>		
$T_{\text{ph}}$	$\sqrt{2\pi} v_x / g$	s
$\zeta$	$C_d / (\sqrt{2} C_l)$ , Eq. (29)	—
<i>Sound generation</i>		
$\omega_i^{\text{AC}}$	$a_j/v_k - a_k/v_j$ (approximate, trajectory-based)	$\text{s}^{-1}$
$S$	$(1/\rho)\nabla \cdot (\rho\boldsymbol{\omega} \times \mathbf{v})$	$\text{s}^{-2}$
<i>Aeroacoustics</i>		
$ p' $	$m d\mathbf{a}/dt /(4\pi cr)$ , Eq. (40)	Pa
SPL	$20 \log_{10}( p' /20 \mu\text{Pa})$	dB
<i>g-loads and turbulence severity</i>		

*continued on next page*

Quantity	Formula / definition	Unit
$n_x$	$a_x/g$	—
$n_y$	$a_y/g$	—
$n_z$	$(a_z + g)/g$	—
$\Delta n$	$n_z - 1$	—
Peak $ \Delta n $	Turbulence severity metric	—
DoD	$\int \sqrt{a_x^2 + a_y^2 + (\Delta n \cdot g)^2} dt$	m/s
<i>Flight dynamics</i>		
IAS	$ \mathbf{v}  \sqrt{\rho/\rho_0}$	m/s
$\gamma_{fp}$	$\arctan(v_z/v_x)$ (not to be confused with $\gamma = c_p/c_v$ )	deg
$\mathcal{T}/(mg)$	Thrust-to-weight ratio	—
$dm/dt$	Fuel burn rate	kg/s
$Re$	$\rho \mathbf{v} C/\mu$ (reference length $C = 6$ m)	—
<i>FFT</i>		
PSD	Hanning-windowed odogram of $z(t)$	peri- m <sup>2</sup> /Hz
$T_{dom}$	$1/f_{peak}$	s

## F Diagnostic Plots

Table 7 catalogues all 28 diagnostic plots generated by `plot_all()`. Each is saved as a PNG file in the specified output directory. An additional conditional plot (`area_fractions`) appears when the area model is used.

Table 7: Complete catalogue of diagnostic plots.

#	Filename	Content and purpose
1	<code>positions</code>	$x(t)$ , $y(t)$ , $z(t)$ . Three subplots. Verifies forward motion, lateral drift, and altitude oscillation.
2	<code>velocities</code>	$v_x(t)$ , $v_y(t)$ , $v_z(t)$ . Shows speed reduction from fuel burn, VT-induced lateral/vertical velocities.
3	<code>accelerations</code>	$a_x(t)$ , $a_y(t)$ , $a_z(t)$ . Shows VT impulse and post-VT oscillation in acceleration space.
4	<code>accel_x_comp.</code>	$x$ -acceleration decomposition: vortex,  drag ,  thrust .
5	<code>accel_y_comp.</code>	$y$ -acceleration decomposition: vortex, friction. Zero for Case 1 ( $\omega_z = 0$ ).
6	<code>accel_z_comp.</code>	$z$ -acceleration decomposition: vortex,  lift ,  gravity , friction. Lift and gravity nearly cancel.
7	<code>z_and_vyz</code>	Two-panel: $z(t)$ and $[v_y, v_z](t)$ . Best single plot for visualising the damped oscillation.

*continued on next page*

#	Filename	Content and purpose
8	g_loads	Four-panel: $n_z$ , $\Delta n$ with severity bands, $[n_x, n_y]$ , cumulative DoD. Key turbulence metrics.
9	atmospheric	Five-panel: $\rho$ , $T$ , $p$ , $\mu$ , $g$ vs. time. All oscillate with altitude.
10	stability	Three-panel: $\theta$ , lapse rate (model vs. dry adiabatic), $d\theta/dz$ .
11	vehicle	Three-panel: mass, thrust, thrust correction factor. Shows TSFC fuel burn.
12	fuel	Two-panel: instantaneous fuel burn rate [kg/s], cumulative fuel burned [kg].
13	energy	Two-panel: (top) $E_{\text{kin}}$ , $E_{\text{pot}}$ , $E_{\text{total}}$ ; (bottom) $\Delta(E_{\text{kin}} + E_{\text{pot}})$ , drag work, damping work, thrust work.
14	energy_detailed	Two-panel: VT work vs. damping losses; energy conservation error.
15	velocity_mach	Two-panel: $ \mathbf{v} $ and Mach number.
16	flight_dynamics	Four-panel: flight path angle, $\mathcal{T}/(mg)$ , IAS vs. TAS, Reynolds number.
17	oscillation_periods	Key physics plot. B-V (526 s), aircraft (181 s), phugoid (101 s), and FFT observed. Title shows $\sqrt{\gamma/(\gamma - n)}$ .
18	bv_calibrated	Trajectory-based B-V periods (calibrated models from draft paper). For backward compatibility.
19	richardson	Richardson number (log scale) with $Ri = 0.25$ instability threshold.
20	vertical_shear	Two-panel: horizontal velocity,  vertical shear  (log scale).
21	phugoid	Phugoid period vs. time. Title shows $\zeta = C_d/(\sqrt{2}C_l)$ .
22	sound_generation	Four-panel (log scale): $ \omega_x $ , $ \omega_y $ , $ \omega_z $ , $ S $ .
23	acoustic_spl	Two-panel: acoustic pressure [Pa] (log), SPL [dB]. Title shows observer distance.
24	acoustic_spectrogram	Three-panel: signed $p'(t)$ , STFT spectrogram with B-V/aircraft/phugoid/hearing threshold marked, instantaneous SPL with infrasound perception threshold.
25	acoustic_spectrogram_zoom	Two-panel zoom around VT encounter: $p'(t)$ and STFT spectrogram showing broadband-to-narrowband transition.
26	fft	Periodogram (Hanning window, log-frequency). Predicted aircraft frequency marked.
27	trajectory_3d	3D trajectory $[x, y, z]$ .
28	vortex_status	VT intersection status (0/1/2 = before/inside/after).

*continued on next page*

#	Filename	Content and purpose
—	<code>area_fractions</code>	(Conditional) Wing/fuselage area fractions, left/right/fwd/aft decomposition.

## G Physics-Derived vs. Configured Parameters

A design goal of this work is to minimise the number of free parameters by deriving as many quantities as possible from fundamental physics.

Table 8: Quantities derived from physics (no free parameters).

Quantity	Formula	Source	Value
$n$ (polytropic)	Eq. (4)	ISA lapse rate	1.2346
$R/c_p$	$(\gamma - 1)/\gamma$	$\gamma = 1.4$	0.2857
$c_p$	$R_{\text{air}}/(R/c_p)$	$R_{\text{air}}, \gamma$	1004.7 J/(kg·K)
$\omega_{\text{ac}}/N_{\text{BV}}$	$\sqrt{\gamma}/(\gamma - n)$	$\gamma, n$	2.909
$T_{\text{aircraft}}$	$2\pi/\omega_{\text{aircraft}}$	Eq. (35)	180.6 s
$\zeta$ (phugoid)	$C_d/(\sqrt{2}C_l)$	Trim state	0.0318
$c_1$ (aero damping)	$\rho v C_d A$	Trim state	912 kg/s

Table 9: Configuration inputs (physical parameters of the scenario).

Parameter	What it is	Default
$\gamma$	Gas property of air	1.4
ISA lapse rate	Defines the atmosphere	−6.5 K/km
TSFC	Engine property	15 mg/(N·s)
$a_g$	VT event severity	0.5
$e$ (Oswald)	Wing efficiency (polar only)	0.8
Vehicle geometry/mass	Aircraft being studied	A330-200

## H Validation

Table 10: Validation of Python (RK4) against MATLAB (Euler) and analytical predictions.

Quantity	MATLAB (Euler)	Python (RK4)	Analytical
Oscillation period [s]	~182	179	181
Max $v_z$ [m/s]	~1.4	1.5	—
Hull volume error	<1%	0.0%	0
B-V calibration ratio	2.893 (fitted)	2.909	2.909
$n$ (polytropic index)	1.235 (input)	1.2346 (derived)	1.2346

## I Errata for Basse (2020)

This appendix addresses a typographical error and two figure-labelling issues in Basse [7].

### I.1 Typographical Error in Equation (4)

**Error:** Equation (4) of [7] defines the total vorticity magnitude as  $\omega_{\text{tot}} \equiv \sqrt{\omega_x^2 + \omega_y^2 + \omega_z^2}$ . The third component under the square root repeats the first.

**Correction:** The third component should be  $\omega_z^2$ :

$$\omega_{\text{tot}} \equiv \sqrt{\omega_x^2 + \omega_y^2 + \omega_z^2}. \quad (44)$$

**Impact:** None. Equation (4) is not used in any subsequent calculation. In the baseline case, only  $\omega_y$  is nonzero, so  $\omega_{\text{tot}} = |\omega_y| = 2\Omega$ . In tilted cases, the individual components enter the cross product directly (Eqs. 22, 26, 30 of [7]).

### I.2 Out-of-Plane Axis Symbol in Figure 3 (Wing Panel)

**Error:** In the wing panel of Figure 3, the positive  $z$ -axis points toward the viewer (out of the page). The correct symbol is  $\odot$ , but  $\otimes$  (into the page) is printed.

**Correction:** The symbol next to the  $z$ -label should be  $\odot$ , not  $\otimes$ . (The fuselage panel's  $\odot$  for the  $y$ -axis is correct.)

**Impact:** None. The coordinate system in all equations is consistently right-handed.

### I.3 Viewing Convention in Figure 2

**Clarification:** Section 2.1 of [7] states “clockwise direction” for the vortex rotation in the  $xz$ -plane without specifying the viewing direction. The rotation is clockwise as seen from above (positive  $z$ -direction) and counterclockwise as seen from  $+y$ . The velocity field  $\mathbf{u} = (-\Omega z, 0, \Omega x)$  (Eq. 2 of [7]) is unambiguous; the verbal description should specify the top-down viewing convention.

**Impact:** None. All derivations use coordinate-component cross products, independent of viewing direction.

### I.4 Summary

All three issues are presentational. Every equation in [7] is formulated in terms of coordinate components and cross products. All analytical results, numerical area fractions and accelerations, and the 17 cases in Table 1 of [7] remain valid as published.

## References

- [1] Sharman, R., Lane, T. (eds) (2016). *Aviation Turbulence: Processes, Detection, Prediction*. Springer.
- [2] Clark, T.L., Hall, W.D., Kerr, R.M., Middleton, D., Radke, L., Ralph, F.M., Neiman, P.J., Levinson, D. (2000). Origins of aircraft-damaging clear-air turbulence during the 9 December 1992 Colorado downslope windstorm. *J. Atmos. Sci.*, 57:1105–1131.
- [3] Roach, W.T. (1970). On the influence of synoptic development on the production of high level turbulence. *Q. J. R. Meteorol. Soc.*, 96:413–429.
- [4] Kaplan, M.L., Huffman, A.W., Lux, K.M., Cetola, J.D., Charney, J.J., Riordan, A.J., Lin, Y.L., Waight, K.T. III (2004). Characterizing the severe turbulence environments associated with commercial aviation accidents. Part 2. *Meteorol. Atmos. Phys.*, 88:153–173.
- [5] Lamb, H. (1932). *Hydrodynamics*, 6th edition. Cambridge University Press.

- [6] Saffman, P.G. (1992). *Vortex Dynamics*. Cambridge University Press.
- [7] Basse, N.T. (2020). Modelling of vortex-induced aviation turbulence. *Meteorol. Atmos. Phys.*, 132:401–411. <https://doi.org/10.1007/s00703-019-00699-0>
- [8] Lunnnon, R. (2016). Turbulence events interpreted by vortex rolls. In: Sharman, R., Lane, T. (eds) *Aviation Turbulence*, Springer, Ch. 4.
- [9] Basse, N.T. (2020). Draft MATLAB code. [https://www.npb.dk/pub/rev1\\_aircraft\\_eq\\_of\\_motion\\_2020.zip](https://www.npb.dk/pub/rev1_aircraft_eq_of_motion_2020.zip)
- [10] Anthropic (2026). Python code generated by Claude Opus 4.6 Extended. <https://doi.org/10.13140/RG.2.2.34706.93121>
- [11] ISO 2533:1975. Standard Atmosphere. International Organization for Standardization.
- [12] Nakayama, Y. (2018). *Introduction to Fluid Mechanics*, 2nd edition. Butterworth-Heinemann.
- [13] Zagarola, M.V. (1996). *Mean-Flow Scaling of Turbulent Pipe Flow*. Ph.D. thesis, Princeton University.
- [14] Lin, Y.-L. (2007). *Mesoscale Dynamics*. Cambridge University Press.
- [15] Sharman, R. (2016). Nature of aviation turbulence. In: Sharman, R., Lane, T. (eds) *Aviation Turbulence*, Springer, Ch. 1.
- [16] Airbus (2019). A330-200 aircraft characteristics, airport and maintenance planning. Airbus S.A.S. <https://www.airbus.com>
- [17] Lanchester, F.W. (1908). *Aerodnetics*. A. Constable & Co.
- [18] Basse, N.T. (2019). Modelling the motion of a point-sized aircraft in response to a vortex tube encounter. Draft manuscript. [https://www.npb.dk/pub/Basse\\_aircraft\\_motion\\_v1.pdf](https://www.npb.dk/pub/Basse_aircraft_motion_v1.pdf)
- [19] Howe, M.S. (2003). *Theory of Vortex Sound*. Cambridge University Press.
- [20] Jacobson, I.D., Kuhlthau, A.R., Richards, L.G., Conner, D.W. (1978). Passenger ride quality in transport aircraft. *J. Aircr.*, 15(10):724–730.
- [21] Zohm, H. (1996). Edge localized modes (ELMs). *Plasma Phys. Control. Fusion*, 38:105–128.
- [22] Connor, J.W., Kirk, A. (2009). Edge Localised Modes (ELMs): experiments and theory. In: *AIP Conference Proceedings*, 1140:349–364.
- [23] Wagner, F. et al. (1982). Regime of improved confinement and high beta in neutral-beam-heated divertor discharges of the ASDEX tokamak. *Phys. Rev. Lett.*, 49:1408–1412.
- [24] García-Muñoz, M. et al. (2025). Effect of energetic ions on edge-localized modes in tokamak plasmas. *Nature Physics*, 21:137–143. <https://doi.org/10.1038/s41567-024-02715-6>
- [25] Storer, L.N., Williams, P.D., Gill, P.G. (2019). Aviation turbulence: dynamics, forecasting, and response to climate change. *Pure Appl. Geophys.*, 176:2081–2095.